

## Charm meson spectra in $e^+e^-$ annihilation at 10.5 GeV c.m.e.

M. Artuso,<sup>1</sup> C. Boulahouache,<sup>1</sup> S. Blusk,<sup>1</sup> J. Butt,<sup>1</sup> E. Dambasuren,<sup>1</sup> O. Dorjkhaidav,<sup>1</sup> J. Haynes,<sup>1</sup> N. Horwitz,<sup>1</sup> N. Menea,<sup>1</sup> G. C. Moneti,<sup>1</sup> R. Mountain,<sup>1</sup> H. Muramatsu,<sup>1</sup> R. Nandakumar,<sup>1</sup> R. Redjimi,<sup>1</sup> R. Sia,<sup>1</sup> T. Skwarnicki,<sup>1</sup> S. Stone,<sup>1</sup> J.C. Wang,<sup>1</sup> Kevin Zhang,<sup>1</sup> A. H. Mahmood,<sup>2</sup> S. E. Csorna,<sup>3</sup> G. Bonvicini,<sup>4</sup> D. Cinabro,<sup>4</sup> M. Dubrovin,<sup>4</sup> A. Bornheim,<sup>5</sup> E. Lipeles,<sup>5</sup> S. P. Pappas,<sup>5</sup> A. Shapiro,<sup>5</sup> A. J. Weinstein,<sup>5</sup> R. A. Briere,<sup>6</sup> G. P. Chen,<sup>6</sup> T. Ferguson,<sup>6</sup> G. Tatishvili,<sup>6</sup> H. Vogel,<sup>6</sup> M. E. Watkins,<sup>6</sup> N. E. Adam,<sup>7</sup> J. P. Alexander,<sup>7</sup> K. Berkelman,<sup>7</sup> V. Boisvert,<sup>7</sup> D. G. Cassel,<sup>7</sup> J. E. Dubosq,<sup>7</sup> K. M. Ecklund,<sup>7</sup> R. Ehrlich,<sup>7</sup> R. S. Galik,<sup>7</sup> L. Gibbons,<sup>7</sup> B. Gittelmann,<sup>7</sup> S. W. Gray,<sup>7</sup> D. L. Hartill,<sup>7</sup> B. K. Heltsley,<sup>7</sup> L. Hsu,<sup>7</sup> C. D. Jones,<sup>7</sup> J. Kandaswamy,<sup>7</sup> D. L. Kreinick,<sup>7</sup> V. E. Kuznetsov,<sup>7</sup> A. Magerkurth,<sup>7</sup> H. Mahlke-Krüger,<sup>7</sup> T. O. Meyer,<sup>7</sup> J. R. Patterson,<sup>7</sup> T. K. Pedlar,<sup>7</sup> D. Peterson,<sup>7</sup> J. Pivarski,<sup>7</sup> D. Riley,<sup>7</sup> A. J. Sadoff,<sup>7</sup> H. Schwarthoff,<sup>7</sup> M. R. Shepherd,<sup>7</sup> W. M. Sun,<sup>7</sup> J. G. Thayer,<sup>7</sup> D. Urner,<sup>7</sup> T. Wilksen,<sup>7</sup> M. Weinberger,<sup>7</sup> S. B. Athar,<sup>8</sup> P. Avery,<sup>8</sup> L. Brevva-Newell,<sup>8</sup> V. Potlia,<sup>8</sup> H. Stoeck,<sup>8</sup> J. Yelton,<sup>8</sup> B. I. Eisenstein,<sup>9</sup> G. D. Gollin,<sup>9</sup> I. Karliner,<sup>9</sup> N. Lowrey,<sup>9</sup> P. Naik,<sup>9</sup> C. Sedlack,<sup>9</sup> M. Selen,<sup>9</sup> J. J. Thaler,<sup>9</sup> J. Williams,<sup>9</sup> K. W. Edwards,<sup>10</sup> D. Besson,<sup>11</sup> K. Y. Gao,<sup>12</sup> D. T. Gong,<sup>12</sup> Y. Kubota,<sup>12</sup> S. Z. Li,<sup>12</sup> R. Poling,<sup>12</sup> A. W. Scott,<sup>12</sup> A. Smith,<sup>12</sup> C. J. Stepaniak,<sup>12</sup> J. Urheim,<sup>12</sup> Z. Metreveli,<sup>13</sup> K. K. Seth,<sup>13</sup> A. Tomaradze,<sup>13</sup> P. Zweber,<sup>13</sup> J. Ernst,<sup>14</sup> K. Arms,<sup>15</sup> E. Eckhart,<sup>15</sup> K. K. Gan,<sup>15</sup> C. Gwon,<sup>15</sup> H. Severini,<sup>16</sup> P. Skubic,<sup>16</sup> D. M. Asner,<sup>17</sup> S. A. Dytman,<sup>17</sup> S. Mehrabyan,<sup>17</sup> J. A. Mueller,<sup>17</sup> S. Nam,<sup>17</sup> V. Savinov,<sup>17</sup> G. S. Huang,<sup>18</sup> D. H. Miller,<sup>18</sup> V. Pavlunin,<sup>18</sup> B. Sanghi,<sup>18</sup> E. I. Shibata,<sup>18</sup> I. P. J. Shipsey,<sup>18</sup> G. S. Adams,<sup>19</sup> M. Chasse,<sup>19</sup> J. P. Cummings,<sup>19</sup> I. Danko,<sup>19</sup> J. Napolitano,<sup>19</sup> D. Cronin-Hennessy,<sup>20</sup> C. S. Park,<sup>20</sup> W. Park,<sup>20</sup> J. B. Thayer,<sup>20</sup> E. H. Thorndike,<sup>20</sup> T. E. Coan,<sup>21</sup> Y. S. Gao,<sup>21</sup> F. Liu,<sup>21</sup> and R. Stroynowski<sup>21</sup>

(CLEO Collaboration)

<sup>1</sup>*Syracuse University, Syracuse, New York 13244*

<sup>2</sup>*University of Texas - Pan American, Edinburg, Texas 78539*

<sup>3</sup>*Vanderbilt University, Nashville, Tennessee 37235*

<sup>4</sup>*Wayne State University, Detroit, Michigan 48202*

<sup>5</sup>*California Institute of Technology, Pasadena, California 91125*

<sup>6</sup>*Carnegie Mellon University, Pittsburgh, Pennsylvania 15213*

<sup>7</sup>*Cornell University, Ithaca, New York 14853*

<sup>8</sup>*University of Florida, Gainesville, Florida 32611*

<sup>9</sup>*University of Illinois, Urbana-Champaign, Illinois 61801*

<sup>10</sup>*Carleton University, Ottawa, Ontario, Canada K1S 5B6*

*and the Institute of Particle Physics, Canada*

<sup>11</sup>*University of Kansas, Lawrence, Kansas 66045*

<sup>12</sup>*University of Minnesota, Minneapolis, Minnesota 55455*

<sup>13</sup>*Northwestern University, Evanston, Illinois 60208*

<sup>14</sup>*State University of New York at Albany, Albany, New York 12222*

<sup>15</sup>*Ohio State University, Columbus, Ohio 43210*

<sup>16</sup>*University of Oklahoma, Norman, Oklahoma 73019*  
<sup>17</sup>*University of Pittsburgh, Pittsburgh, Pennsylvania 15260*  
<sup>18</sup>*Purdue University, West Lafayette, Indiana 47907*  
<sup>19</sup>*Rensselaer Polytechnic Institute, Troy, New York 12180*  
<sup>20</sup>*University of Rochester, Rochester, New York 14627*  
<sup>21</sup>*Southern Methodist University, Dallas, Texas 75275*

(Dated: May 22, 2019)

## Abstract

Using the CLEO detector at the Cornell Electron-positron Storage Ring, we have measured the momentum spectra and the total inclusive production cross sections of the charm mesons  $D^+$ ,  $D^0$ ,  $D^{*+}$  and  $D^{*0}$  in  $e^+e^-$  annihilation at about 10.5 GeV center of mass energy. The statistical accuracy and momentum resolution are superior to previous measurements at this energy.

PACS numbers: 13.66.Bc, 13.87.Fh, 14.40.Lb, 14.65.Dw

## I. INTRODUCTION

We report the measurement of the momentum spectra of charged and neutral  $D$  and  $D^*$  charm mesons produced at the Cornell Electron-positron Storage Ring, CESR, in non-resonant  $e^+e^-$  annihilation at about 10.5 GeV center of mass energy (CME) and observed with the CLEO detector. From them we also derive the total, inclusive production cross section for these charm mesons.

While very accurate data on bottom quark production from LEP and SLD have been published in recent years [1, 2, 3, 4], the data currently available for studies of charm fragmentation at 10.5 GeV CME [5, 6], are quite old and, by present standards, of poor statistical quality and momentum resolution. Our statistical sample is about 80 times larger than the our previous one [6] and our current momentum resolution is about a factor of 2 better.

The spectra represent measurements of charm quark fragmentation distributions  $D_c^h(x, s)$ , *i.e.*, the probability density that a  $c$  quark produces a charm hadron  $h$  carrying a fraction  $x$  of its momentum,  $\sqrt{s}$  being the “energy scale” of the process, the  $e^+e^-$  CME in our case [7, 8]. Experimental heavy meson spectra in  $e^+e^-$  collisions are important for theoretical and practical reasons: (i) they provide a component that is not yet calculable in predicting heavy flavor production in very high energy hadronic collisions, (ii) they can test advanced perturbative QCD (PQCD) methods, (iii) they can test the QCD evolution equations, and (iv) they provide information for best parametrization of the Monte Carlo simulations on which the analysis of many high energy experiments partially rely.

Items (i) and (ii) are strictly interconnected. The calculations of heavy flavor production cross sections in hadronic collisions (*e.g.*, at the Tevatron and the LHC) are generally based on the factorization hypothesis, *i.e.*, a convolution of (a) the parton distribution function for the colliding hadrons, (b) the perturbative calculation of the parton-parton cross section and (c) the parton fragmentation function  $D_q^h(x, s)$ . Items (b) and part of (c) (the parton-shower cascade) can be calculated, in the case of heavy quarks, using PQCD. Items (a) and the second phase of (c) (the hadronization phase) are intrinsically non-perturbative (long distance) processes: as of now, they must be provided by experiments. There is an ongoing theoretical effort to push the potential of PQCD to calculate the perturbative component of the fragmentation function. It needs tests and guidance from the experimental spectra of heavy flavored hadrons produced in  $e^+e^-$  annihilation. De-convoluting the calculated PQCD component from the experimental spectra one obtains the non-perturbative component of the fragmentation function. Unphysical behaviour of the result (*e.g.*, negative values, extension beyond the kinematical limit) is indication that further refinement of the PQCD calculation is needed. Tests of this kind have been performed up to now on data of  $B$  production in  $e^+e^-$  annihilation [9, 10] as well as in hadronic collisions [11, 12], and on charm production also in hadron collisions [13] and in  $ep$  collisions [14, 15]. Charm production in  $e^+e^-$  annihilation provides a new testing ground of these theoretical attempts [16]. The larger value of  $\Lambda_{QCD}/m_c$  with respect to  $\Lambda_{QCD}/m_b$  makes these non-perturbative effects more evident than in bottom hadron production.

Tests of the Altarelli-Parisi evolution equations [17, 18] have been performed by our collaboration [6] with low sensitivity and over a relatively small energy interval, comparing the CLEO results with PETRA results. The spectra reported in the present paper can be compared with LEP [19] results providing a test over the 10 to 200 GeV energy range.

Lacking rigorous calculations of the process of quark and gluon hadronization, QCD in-

spired Monte Carlo simulations have been built: the Lund String Model [20, 21, 22] and Cluster Fragmentation [23]. These models have been implemented in Monte Carlo programs (JETSET [24], UCLA[25], HERWIG [23]). In each case a number of parameters are introduced, to be determined by fitting the experimental distributions. Monte Carlo simulations of quark hadronization are used by experiments to determine detection efficiencies and to calculate some sources of backgrounds. The results presented here include a JETSET parametrization that produces spectra that agree quite well with the shapes of all spectra obtained in this analysis.

Since in all these uses of our results, what is important is the shape of the spectra, rather than the absolute values of the cross sections, shape is the focus of our attention.

In Sec. II we first list the charm mesons studied in our analysis along with the decay modes considered and then we describe the data sample analyzed and the procedures used to produce the spectra. In Sec. III the results, *i.e.*, the charm meson spectra, are shown in the order given in Sec. II A. Our results for the total, inclusive production cross sections are given in Sec. IV. Our optimization of the JETSET parameters to reproduce our spectra is described in Sec. V. In two appendices we show plots of the detection efficiencies for the mesons observed and provide detailed tables of the measured spectra.

## II. ANALYSIS SCOPE AND PROCEDURES

### A. Charm mesons and decay modes considered

We measure the momentum distribution of  $D^+$ ,  $D^0$ ,  $D^{*+}$  and  $D^{*0}$  using the following decay modes (charge conjugates are implied throughout this paper):

- $D^+$

$$D^+ \rightarrow K^- \pi^+ \pi^+$$

- $D^0$

$$D^0 \rightarrow K^- \pi^+$$

$$D^0 \rightarrow K^- \pi^+ \pi^+ \pi^-$$

- $D^{*0}$

$$D^{*0} \rightarrow D^0 \pi^0 \rightarrow (K^- \pi^+) \pi^0$$

$$D^{*0} \rightarrow D^0 \pi^0 \rightarrow (K^- \pi^+ \pi^+ \pi^-) \pi^0$$

- $D^{*+}$

$$D^{*+} \rightarrow D^0 \pi^+ \rightarrow (K^- \pi^+) \pi^+$$

$$D^{*+} \rightarrow D^0 \pi^+ \rightarrow (K^- \pi^+ \pi^+ \pi^-) \pi^+$$

The use of different decay modes of the same meson provides a check on possible systematic biases.

## B. Data Sample and Detector

The data sample of  $e^+e^-$  annihilations used in this study was taken with the CLEO II.V detector [26, 27] at CESR during 1995–1999. The sample consists 2.9 fb<sup>-1</sup> of “continuum” (i.e., non-resonant)  $e^+e^-$  annihilation (at about 10.52 GeV, i.e., 36 MeV below  $B\bar{B}$  threshold) and the “ON4S” sample, i.e., 6.0 fb<sup>-1</sup> of  $e^+e^-$  annihilation at about 10.58 GeV, the  $\Upsilon(4S)$  resonance peak. Both samples are used for charm mesons with momenta above the maximum kinematically allowed in  $B$  decay. For lower momenta, we use only the continuum sample, reducing the statistics available in that region. All charm hadrons coming from  $B$  decays are thus excluded.

## C. Selection Criteria

We select events using standard CLEO criteria designed to efficiently select  $e^+e^-$  annihilation into hadrons, while rejecting Bhabha scattering,  $e^+e^- \rightarrow \mu^+\mu^-$ , and beam-gas interactions. At least three tracks are required. Events with three or four tracks must also have 65% of the center-of-mass energy deposited in the calorimeter. Those with five or more tracks must have total visible energy, summing both energy in tracks and neutral energy in the calorimeter, more than 20% of the center-of-mass energy.

Tracks used to reconstruct a  $D$  or  $D^*$  are required to be the result of good tracking fits and have an angle with respect to the beam line,  $\theta$ , such that  $|\cos\theta| < 0.91$ . They are also required to be consistent with originating from the luminous region. Further if they have momentum greater than 250 MeV/ $c$  we require that the impact parameter with respect to the beam line be less than 3 mm, and that the distance between the point of closest approach to the beam line and the event vertex be less than 2.5 cm.

Particle identification requirements are imposed based on the specific ionization (dE/dx) and time of flight measurements for the track. The requirement is that the combined  $\chi^2$  probability of the chosen identification be greater than 4%.

Photon candidate showers detected in the central barrel region ( $|\cos\theta| < 0.707$ ) of the crystal calorimeter are required to have a minimum energy of 30 MeV. Those detected in the forward calorimeters are required to have a minimum energy of 50 MeV. Photon candidates are also required to be well separated from the extrapolated position of all tracks, and the lateral shape of the energy distribution should be consistent with that expected from an electromagnetic shower.

Candidate  $\pi^0$  mesons are reconstructed from pairs of photon candidates. At least one of the two must be in the central barrel region. If the invariant mass of the photon pair is less than 2.58 standard deviations from the expected  $\pi^0$  mass, the combination is kinematically fitted to the nominal  $\pi^0$  mass. The combination is accepted if this fit has  $P(\chi^2) \geq 0.10$  and then its fitted 4-momentum is used in  $D^{*0}$  reconstruction.

## D. Candidate mass distribution fitting

For the  $D^+$  and  $D^0$  analyses we select candidate daughters, add their four-momenta and calculate the invariant mass  $M_{cand}$  of the charm meson. Multiple candidates in the same event are accepted. We construct histograms of  $M_{cand}$  in 0.05 wide bins of  $x_p(D) \equiv$

$p/p_{max}$ , where  $p_{max}$  is the maximum attainable momentum at the relevant beam energy, approximately 4.95 GeV/c.

In the “ON4S” sample we eliminate charm mesons from B decays by requiring  $x_p > 0.50$ . To combine the two parts of the spectra,  $x_p < 0.50$  which we extract from only the continuum sample, and  $x_p > 0.50$  which we extract from both the continuum and “ON4S” samples, we scale the  $x_p < 0.50$  spectra by the ratio of integrated luminosities of the two samples. Also we account for the dependence of the  $e^+e^-$  annihilation cross section on the inverse square of the CME. The statistical sample for  $x_p < 0.50$  is a factor of three smaller than that for  $x_p > 0.50$ .

In the  $D^*$  case we obtain the  $M_{cand}$  distribution for the  $D^0$  associated with the  $D^*$  by selecting  $D^*$  candidates with  $Q \equiv M_{cand}^* - M_{cand} - m_\pi$  in the signal region for  $D^*$  decay. Here  $M_{cand}^*$  is the invariant mass of the decay products of the candidate  $D^*$ . Random  $D$ - $\pi$  associations are subtracted using the  $M_{cand}$  distribution for events in the side bands of the  $D^*$  signal in the  $Q$  distribution.

Fig. 1 shows three examples of the  $M_{cand}$  distributions for events with  $Q$  in the signal region and for those in the  $Q$  side bands. The residual background after the subtraction is due to  $D$  candidates from random track association.

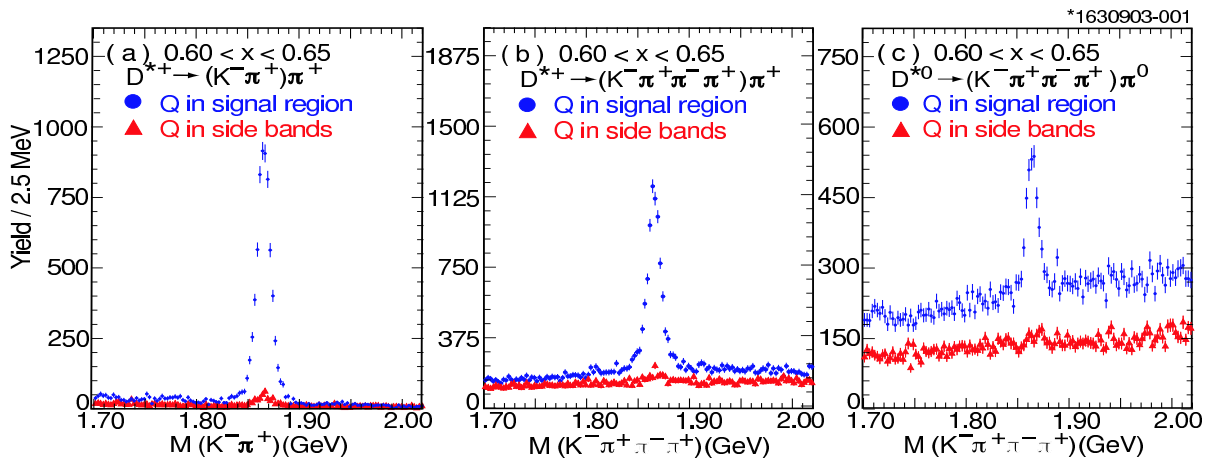


FIG. 1: Examples of  $M_{cand}$  distribution for two  $D^{*+}$  decay channels and one of the  $D^{*0}$  channels analyzed. (a)  $D^{*+} \rightarrow (K^- \pi^+) \pi^+$ . (b)  $D^{*+} \rightarrow (K^- \pi^+ \pi^- \pi^+) \pi^+$ . (c)  $D^{*0} \rightarrow (K^- \pi^+ \pi^- \pi^+) \pi^0$ . They show the  $M_{cand}$  distribution for  $Q$  in the  $D^{*+}$  signal region and for  $Q$  in the  $D^{*+}$  side bands.

The choice of the signal shape used to fit the  $M_{cand}$  distribution was studied and discussed in detail in a previous paper [28]. A Gaussian function does not give a sufficiently accurate parametrization of the  $D$  signal. Track measurement errors vary because of the geometrical orientation of the  $D$  decay products in the detector, because of different momenta of the decay tracks and overlap with other tracks. That study concluded that a satisfactory choice for the  $D$  signal shape is a double Gaussian, *i.e.*, two Gaussians constrained to have the same mean. A different choice of signal fitting function is the signal shape obtained from the Monte Carlo simulation where, for each track, we can identify the input particle that generated it. We call the signal mass histograms thus obtained (one for each momentum bin) the “TAGMC shape”. For this choice we repeat a test that was performed in the previous paper [28], on the  $D^0 \rightarrow K^- \pi^+$  channel, as follows.

We perform the  $D^0$  analysis just replacing the double Gaussian with the TAGMC shape. With this signal shape we obtain excellent fits, although not superior to the double Gaussian

fits. The two spectra are compared in Fig. 2(a) after normalizing one to the other. The normalization factor is  $1.016 \pm 0.007$ . In Fig. 2(b) we show the bin-by-bin fractional difference between the two spectra. There is no  $x_p$  dependence of the difference and it is consistent with no difference between the two choices of shape at the 91.0% Confidence Level. Since  $D^*$  signals are extracted from  $D^0$  candidate mass distributions the same signal shape are used and the test result applies also to the  $D^*$  analysis.

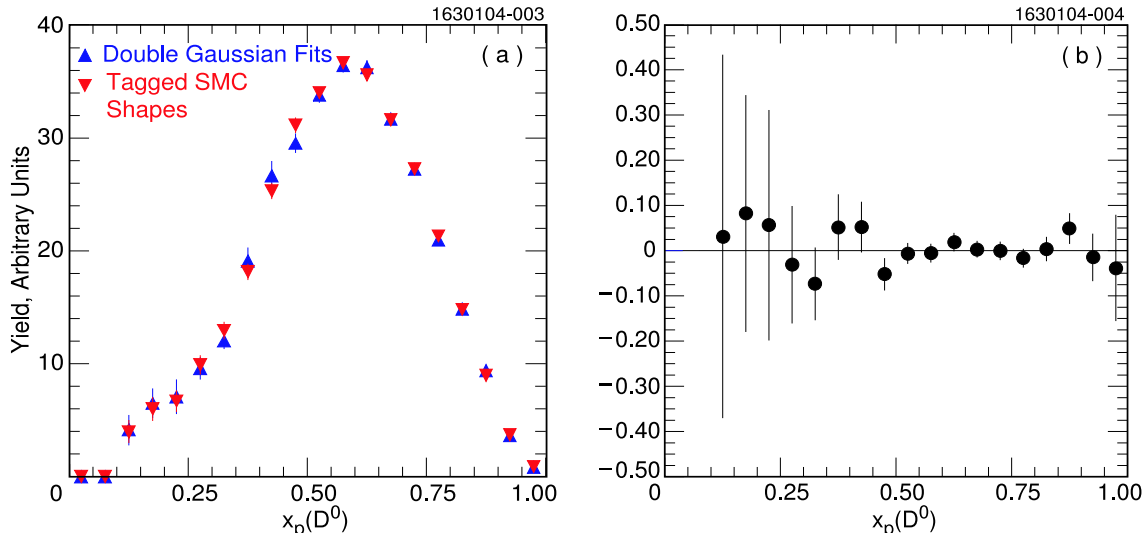


FIG. 2: (a) Overlay of  $D^0$  spectra from double Gaussian and TAGMC shape signal fitting; (b) fractional difference of the two spectra.

The suitability of the double Gaussian as fitting function is also confirmed by the goodness of the fits: in all the channels, the fit confidence levels are evenly distributed between 0.0 and 1.0, as they should be. A quadratic polynomial is used to fit the combinatoric background.

The fits of the  $M_{cand}$  distributions are over the whole 1.70-2.02 GeV range shown in the figures, except for the  $D^+ \rightarrow K^- \pi^+ \pi^+$  case, where we exclude the 1.96-2.02 GeV ( $D^{*+}$ ) region, and for the  $D^0 \rightarrow K^- \pi^+$  case, as explained in the next subsection. The fitted area of the double Gaussian (or the result of the COUNT procedure described in Sec. IID 2) is the “raw” yield for that  $x_p$  bin.

In the next two subsections, we discuss additional backgrounds in the  $M_{cand}$  distribution from the  $D^0 \rightarrow K^- \pi^+$  channel, and describe an alternative procedure, the COUNT method, of estimating the raw yield in the  $D^0 \rightarrow K^- \pi^+ \pi^- \pi^+$  channel.

### 1. The $D^0 \rightarrow K^- \pi^+$ case

In the  $D^0 \rightarrow K^- \pi^+$  case (direct or from  $D^{*+}$  decay) additional backgrounds must be considered:  $D^0$  decays to  $K^- K^+$ ,  $\pi^- \pi^+$ ,  $K^- \rho$  and  $\bar{D}^0 \rightarrow K^+ \pi^-$  misinterpreted as  $K^- \pi^+$ . The shape of their  $M_{cand}$  distributions are obtained from Monte Carlo simulation.

The  $K^- \rho^+$  background is very small and contributes to only the  $1.70 < M(K^- \pi^+) < 1.75$  GeV mass region. This contribution is excluded by not considering this mass region in the fit.

The background due to  $K\pi$  switched identities shows as a very broad enhancement centered at the signal position. For  $x_p > 0.20$ , this enhancement is so broad that it can be easily accommodated by the quadratic term of the polynomial background function. For

small  $x_p$ , it is narrower, but contributes negligibly. The amount of this background is fixed to a momentum dependent fraction determined by Monte Carlo simulation.

The backgrounds due to  $D^0$  decays to  $K^-K^+$ ,  $\pi^-\pi^+$  do not contribute to the peak, but, if ignored, would result in very poor fit of the background. Such a fit overestimates the amount of background under the signal and thus underestimates the amount of signal. The  $D^0 \rightarrow K^-K^+$  background level is a parameter to be fitted. Because of lack of statistics, the amount  $D^0 \rightarrow \pi^-\pi^+$  background is constrained to a fixed fraction (0.357) of the  $D^0 \rightarrow K^-K^+$  background, based on the known relative branching ratio [29]. The  $\pi\pi$  contribution is very small, and alternative methods of accounting for it cause negligible changes in signal yields.

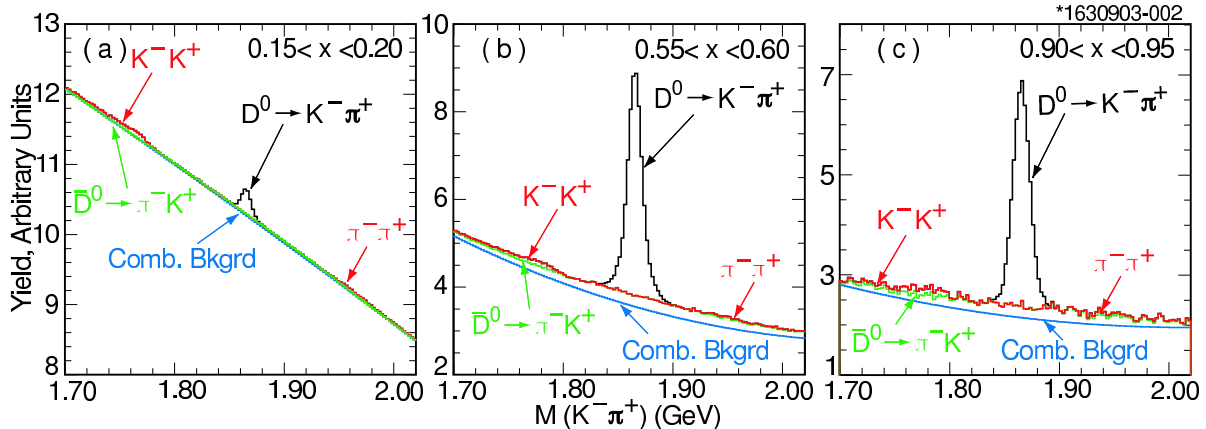


FIG. 3: Build up of the background from its components (plus the signal) in the  $M(K^-\pi^+)$  distribution. Notice the offset on the yield axis.

Fig. 3 shows, in three representative momentum intervals, the background built up from the four contributions.

## 2. The $D^0 \rightarrow K^-\pi^+\pi^+\pi^-$ case: the COUNT method

In the case of the  $D^0 \rightarrow K^-\pi^+\pi^+\pi^-$  decay, direct or from  $D^*$  decay, in addition to the procedure of fitting the signal with a double Gaussian, we used a different procedure that leads to results that are statistically competitive with the double Gaussian fitting. Since, in this case, the background is very smooth over a wide  $M_{cand}$  region and the signal is quite narrow, we fit the background to a polynomial excluding the signal region. We then count the events in the signal region and subtract the background extrapolated from the fit in the surrounding region.

The signal region is centered on the mean of the double Gaussian fit, and its range (1.820-1.910 GeV) is visually judged from the double Gaussian fits to safely contain the whole signal. We repeat the procedure using the exclusion regions 1.810-1.920 GeV and 1.830-1.900 GeV. We use the “gMC check”, described in Sec. III, to choose the best among the three exclusions. The 1.820-1.910 GeV exclusion gives the best gMC check confidence level: 28%. The narrower exclusion gives the worst C.L.: 6%. The wider exclusion gives an acceptable C.L., 22%, but that is, in part, because the wider the exclusion region is, the larger the statistical error becomes. The three yields are used to estimate the systematic error of this procedure.

## E. Detection Efficiency

The detection efficiency is estimated by Monte Carlo simulation. We generate non-resonant  $e^+e^- \rightarrow q\bar{q}$  annihilation events using the JETSET 7.3 [30] package. The events are then processed through a GEANT-based [31] simulation of the CLEO detector, reconstructed and analyzed as real data, according to the procedures described above.

We use two kinds of Monte Carlo simulations. In the first, called “signal Monte Carlo” (sMC), only  $e^+e^- \rightarrow c\bar{c}$  events are generated at the JETSET stage, and an event is accepted only if the charm meson under study is present. That meson is made to decay only in the mode under study. The corresponding antimeson decays generically. We produce three sMC’s, one for  $D^+$  and two for  $D^0$  for the two decay channels analyzed. Some of the  $D$ ’s in these Monte Carlo’s are directly produced, while other ones are daughters of  $D^*$ , hence these Monte Carlo’s are also used to estimate the  $D^*$  detection efficiency. In the second kind of simulation, the “generic Monte Carlo” (gMC), all possible  $e^+e^-$  hadronic annihilations are produced according to present knowledge [29].

Signal Monte Carlo’s and generic Monte Carlo accurately reproduce the  $D$  and  $D^*$  signal shapes in data. Backgrounds in the signal Monte Carlo’s are much smaller than those in the generic Monte Carlo, which fairly simulates the backgrounds in the data.

For each  $D$  or  $D^*$  meson and its decay chain, we find the sMC and gMC efficiencies to be statistically compatible, proving that the strong background reduction in the sMC does not affect the efficiency estimation or, vice versa, that the large background of the gMC does not introduce any appreciable bias error. We can then reduce the statistical error on the detection efficiency by taking the weighted average of the two.

The detection efficiency should be a smooth function of  $x_p$ . We fit with a second order polynomial the  $x_p$  dependence of the detection efficiency averaged over the signal and generic Monte Carlo. Adding a cubic term does not improve any of the fits. We call the result of this fit the “smoothed efficiency”. In Appendix A, we show the detection efficiency dependence on  $x_p$  for all the mesons and decay modes analyzed. In Figs. 23, 24, 25, the detection efficiencies obtained from the signal and generic Monte Carlo’s are plotted, and the curve resulting from the fit of their average to a polynomial is overlaid.

The detection efficiency corrected spectrum is obtained dividing the raw signal yield by the smoothed efficiency, bin-by-bin in  $x_p$ .

## F. Fit parameter smoothing

The shape parameters of the signal and background functions are expected to depend smoothly on  $x_p$ . By imposing this smoothness of the shape parameters we suppress, in part, the bin-to-bin (in  $x_p$ ) statistical fluctuations in the spectra, thus improving the accuracy of the *shape* of the spectra, particularly at low  $x_p$  where statistics are poor. In the last paragraph of this section we show the extent of improvement obtainable.

The parameters considered are: the mean of the double Gaussian (common to the two Gaussians), the width of the narrower Gaussian,  $\sigma_1$ , the ratio of the widths of the wider to the narrower Gaussian,  $\sigma_2/\sigma_1$ , and the ratio of the area of the wider Gaussian to the total area,  $A_2/A_{tot}$ . We impose this smooth behavior by fitting the  $x_p$  dependence of each shape parameter to a polynomial, at most quadratic, in  $x_p$ .

We proceed in stages. We start by smoothing the parameter that shows the least fluctuations and repeat the  $M_{cand}$  distribution fitting for all the  $x_p$  bins, fixing that parameter to

the value given by the smoothing function. We do this in sequence for all shape parameters. If a parameter does not show appreciable statistical fluctuations, we may skip smoothing it. It may take up to five iterations to smooth all the parameters.

At each stage we get a new  $x_p$  spectrum and check that we have not introduced any distortion to that spectrum. The check is performed by calculating the bin-by-bin ratio of the new spectrum to the original one where all the parameters were allowed to float (the “no smoothing” spectrum). This ratio should show only random fluctuations around unity. If the ratio shows any trend vs  $x_p$ , *e.g.*, if a slope and/or a curvature is needed to describe the  $x_p$  dependence of the ratio, that smoothing stage is discarded. Fig. 4 shows three examples of these checks. When we fit the ratios to a constant, unit ratio, we obtain CL of 94.6%, 91.0% and 38.0% respectively for the three examples shown. These are typical for all the retained smoothing steps.

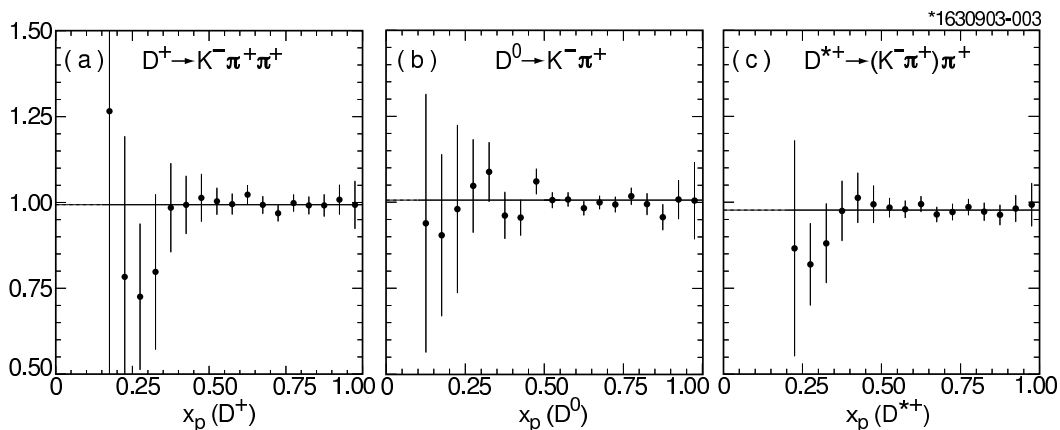


FIG. 4: Ratio of the spectrum after double Gaussian shape parameter smoothing to the one obtained without smoothing: (a)  $D^+ \rightarrow K^- \pi^+ \pi^+$ , (b)  $D^0 \rightarrow K^- \pi^+$ , (c)  $D^{*+} \rightarrow (K^- \pi^+) \pi^+$ .

There is a certain amount of arbitrariness in the smoothing procedure. Complete smoothing of all the parameters is performed using different sequences of the smoothing stages. Comparison of spectra derived from different smoothing sequences provides a measure of the associated systematic error, as explained in Sec. II J.

We use the two independent Monte Carlo simulations discussed in Sec. II E to see if the smoothing procedure improves the agreement between the reconstructed and the original spectrum, *i.e.*, the spectrum that is the input to the Monte Carlo simulation. We use the gMC as data, correct for detection efficiency the spectrum obtained from its analysis using the detection efficiency estimated using the sMC, and fit the spectrum so corrected to the original spectrum. We can then see if the smoothing procedure improves the agreement between reconstructed and original spectrum. The agreement is measured by the confidence level (CL) of fitting one with the other. We observe an improvement in all channels where parameter smoothing was feasible. For example, in the  $D^0 \rightarrow K^- \pi^+$  case the the CL changes from 5% to 95%, in the case of  $D^+ \rightarrow K^- \pi^+ \pi^+$ , the CL improves from 7% to 13%, in the  $D^{*+} \rightarrow (K^- \pi^+) \pi^+$  case, where the CL is already 93% without parameter smoothing, there still is a small improvement to 97%. As expected, the improvement is strong when the initial set of parameters show large fluctuations, smaller when the parameters show a fairly smooth behaviour even before any smoothing.

## G. Momentum Resolution

Comparison with theoretical calculation may involve the moments of the spectra:  $\int_0^1 x^N \frac{d\sigma}{dx} dx$ . It is then important to know the momentum, and hence the  $x_p$ , resolution in our analysis. Using the CLEOG Monte Carlo simulation [31], which reproduces rather accurately our track and shower measuring errors, we plot the difference between  $x_p$  measured and  $x_p$  input (from JETSET). Fig. 5 shows this resolution distribution for the mode  $D^0 \rightarrow K^- \pi^+$  for all momenta. The full width at half maximum (FWHM) is 0.008, *i.e.*, 16% of the bin size (0.050). The resolution (FWHM) varies monotonically with momentum, from 4% of bin size at  $x_p = 0.10$  to 18% for  $x_p = 0.95$ . For the other channels the resolution is likewise a small fraction of the bin size.

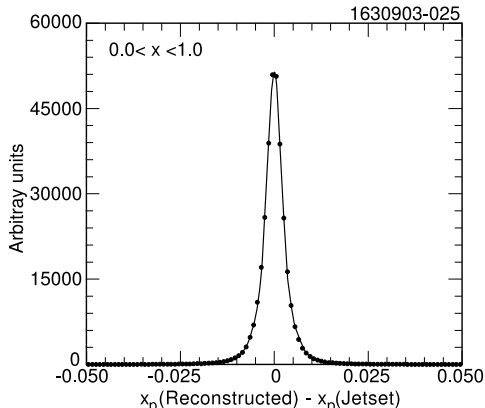


FIG. 5: Resolution in  $x_p$  for the  $D^0 \rightarrow K^- \pi^+$  channel. All momenta.

## H. The Final or Combined Spectrum.

For each  $D$  or  $D^*$  meson and its decay chain, we obtain spectra using four or five variations of the procedures. When fitting the signal with a double Gaussian the variations are: (i) no parameter smoothing and (ii) different order of the stages of the smoothing procedure. We then take as our result the bin-by-bin simple average of the latter.

When we also employ the COUNT method, we use the bin-by-bin simple average of the spectrum obtained by double Gaussian fitting and the one obtained by the COUNT method, with the nominal choice of the signal region:  $1.820 < M_{cand} < 1.910$  GeV.

## I. Checks

In the  $D^0$ ,  $D^{*+}$  and  $D^{*0}$  cases we obtain the respective spectra from two different  $D^0$  decay modes. When the spectrum from one decay mode is fit to the spectrum from the other, we obtain, respectively, the following CL: 93%, 100% and 94%. The statistical agreement of the two decay modes is a good test of our procedures.

By dividing the sum over all bins of the uncorrected spectrum by the corresponding sum of the detection-efficiency-corrected spectrum, we get the average detection efficiency for each channel. The appropriate roots of these efficiencies and the ratios between them provide six different ways to estimate the single-track average detection efficiency. The six values turn out to be statistically compatible and average to  $0.773 \pm 0.007$ .

The two statistically independent Monte Carlo simulations allow an internal check of our procedures and an estimate of the systematic errors. We (i) analyze the gMC as data, (ii) correct the reconstructed spectrum using the efficiency obtained from the sMC, and (iii) compare this efficiency-corrected spectrum with the JETSET generated spectrum that is the input to the gMC. This comparison is performed by using the input spectrum as a “function histogram” to fit the reconstructed spectrum. The only parameter is the relative normalization. The resulting  $\chi^2$  probability, or confidence level, is the measure of the goodness of the check. This “gMC check” resulted in satisfactory CL for all the analyzed channels, as shown in Table I.

TABLE I: Confidence levels of the fit of the gMC reconstructed spectrum with its input spectrum (gMC check) for the seven decay channels analyzed.

Decay channel	Conf. Level (%)	Decay channel	Conf. Level (%)
$D^+ \rightarrow K^- \pi^+ \pi^+$	13	$D^{*+} \rightarrow (K^- \pi^+) \pi^+$	97
$D^0 \rightarrow K^- \pi^+$	95	$D^{*+} \rightarrow (K^- \pi^+ \pi^+ \pi^-) \pi^+$	71
$D^0 \rightarrow K^- \pi^+ \pi^+ \pi^-$	20	$D^{*0} \rightarrow (K^- \pi^+) \pi^0$	86
		$D^{*0} \rightarrow (K^- \pi^+ \pi^+ \pi^-) \pi^0$	99

## J. Statistical and Systematic Errors

The statistical errors on the raw spectra are taken to be those obtained in the  $M_{cand}$  fitting when all fitting parameters are free to float (“no smoothing” case). The statistical errors on the efficiency corrected yield are the combination of the statistical error on the raw yield and the efficiency statistical error. The latter are always considerably smaller than the former.

Two systematic errors affect the shape of the spectra. To take into account the four or five variations of the procedures described in the previous subsection and in Sec. II F, we calculate the root-mean-square (rms) spreads of the yields for each  $x_p$  bin. Since these rms spreads fluctuate statistically from bin to bin, as expected, we average them over groups of a few bins. We take these rms spreads as systematic errors on the yields.

The gMC check described in the previous subsection is also used to estimate an additional systematic error in our analyses. We take the bin-by-bin difference of the normalized, reconstructed spectrum and the input spectrum, and divide this, bin-by-bin, by the input spectrum, resulting in the distribution of the fractional difference vs  $x_p$ . The weighted average, over the entire  $x_p$  range, of the absolute values of these fractional differences (where the weights are the inverse square errors on the differences) can be considered as an estimate of the systematic error. It varies from 0.6% for the  $D^0 \rightarrow K^- \pi^+$  channel to 1.4% for the  $D^+ \rightarrow K^- \pi^+ \pi^+$  channel. The distributions of the fractional differences show negligible dependence on  $x_p$ , meaning that this estimated systematic error does not seem to affect the shape of the spectra. Nevertheless we include these average differences as a component of the systematic error on the measured yields.

Since, in the gMC check, the comparison is with the input spectrum, this systematic error includes all sources of systematic error on the shape of the spectra except possible errors in GEANT track and shower reconstruction that are common to signal and generic Monte Carlo.

The statistical errors and the two systematic errors just described are listed, channel by channel, in Table V - XI in Appendix B. The systematic errors are generally appreciably smaller than the statistical ones. These three errors, statistical and systematic, are combined in quadrature to give total errors relevant to the shape of our spectra.

The test that uses a signal fitting function other than a double Gaussian, as described in Sec. IID, gives us a measure of the sensitivity of our results to the choice of signal fitting function. Based on the different normalization of the two fitting choice, we attribute a systematic error of 1.6% from the choice of signal fitting function. Since that test showed no momentum dependence of the difference between the two methods, we attribute this systematic error to the total cross sections, but not to the spectra shapes.

We have considered the possibility of swapping between a background that is highly curved in the signal region, and the wide component of the double Gaussian. The only two channels that show an appreciable background curvature are the  $D^0 \rightarrow K^- \pi^+ \pi^+ \pi^-$  and  $D^+ \rightarrow K^- \pi^+ \pi^+$ . In the first case the full compatibility of the fits with the results of the COUNT procedure, described in a previous subsection IID 2, shows that this swapping, if it exists, is much smaller than the statistical error. In the  $D^+$  case we performed the same test with the same result, although with poorer statistical accuracy.

We have considered the possibility that inaccurate simulation of initial state radiation (ISR) may have introduced a systematic error in our estimate of the detection efficiencies. We compare the detection efficiencies discussed in Sec. IIE with those obtained from Monte Carlo events where no ISR was produced. As expected, the latter is slightly higher than the former, but only by 1.1%. Since our Monte Carlo does simulate the initial state radiation, the uncertainty is only in the accuracy of the simulation. We thus take half of that, 0.5% as contribution to the systematic error on the cross sections; it will be taken into account in Sec. IV. Since the momentum dependence of this difference in efficiencies is found to be negligible, this possible error does not affect the shape of the spectrum, the main purpose of our analysis.

Additional systematic errors that affect only the normalization of the spectra to the differential cross section, but do not affect its shape, will be discussed in Sec. IV on total cross sections.

### III. RESULTS

The spectra shown in the following are differential, inclusive production cross sections,  $d\sigma(e^+e^- \rightarrow D^{(*)}X)/dx_p$ , fully corrected for detection efficiency and decay branching ratios. We use the following decay branching ratios:  $\mathcal{B}(D^0 \rightarrow K^- \pi^+) = 3.82\%$ ,  $\mathcal{B}(D^0 \rightarrow K^- \pi^+ \pi^- \pi^+) = 7.49\%$ ,  $\mathcal{B}(D^+ \rightarrow K^- \pi^+ \pi^+) = 9.0\%$ ,  $\mathcal{B}(D^{*+} \rightarrow D^0 \pi^+) = 67.59\%$ ,  $\mathcal{B}(D^{*0} \rightarrow D^0 \pi^0) = 61.9\%$ . They affect only the normalization, not the shape, of the spectra. Their effect and the related errors will be discussed in Sec. IV.

For each  $D$  or  $D^*$  meson and its decay chain, we choose the spectrum obtained with the procedure that we consider most reliable, as specified in each case.

## A. $D^+$ Spectrum

Fig. 6 shows examples of fits to the  $M_{cand}$  distributions in three representative  $x_p$  bins, using fully smoothed parameters. Our result is shown in Fig. 7 and tabulated in App. B, Table V, where the two systematic errors are listed. The spectrum shown is obtained after smoothing the  $x_p$  dependence of the double Gaussian shape parameters and gives the best CL in the gMC check (Sec. III).

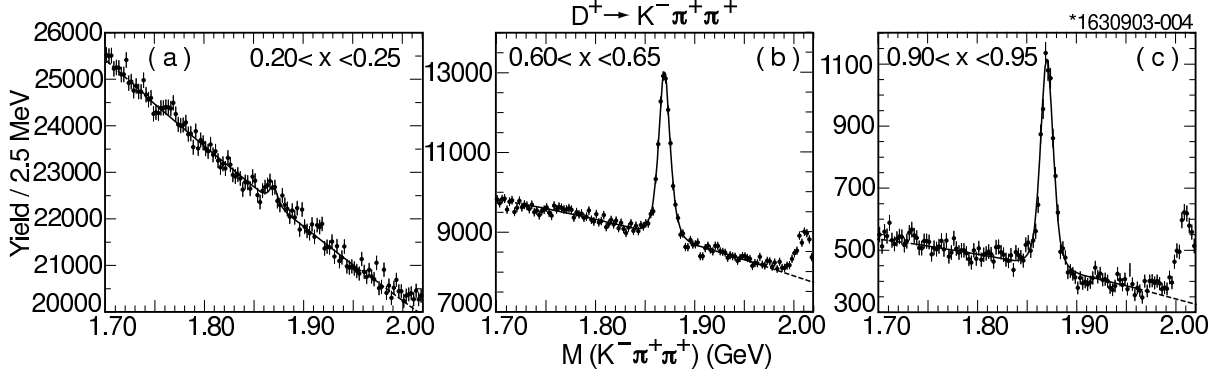


FIG. 6: Three examples of  $M(K^-\pi^+\pi^+)$  distribution fits. Notice the large vertical scale offsets.

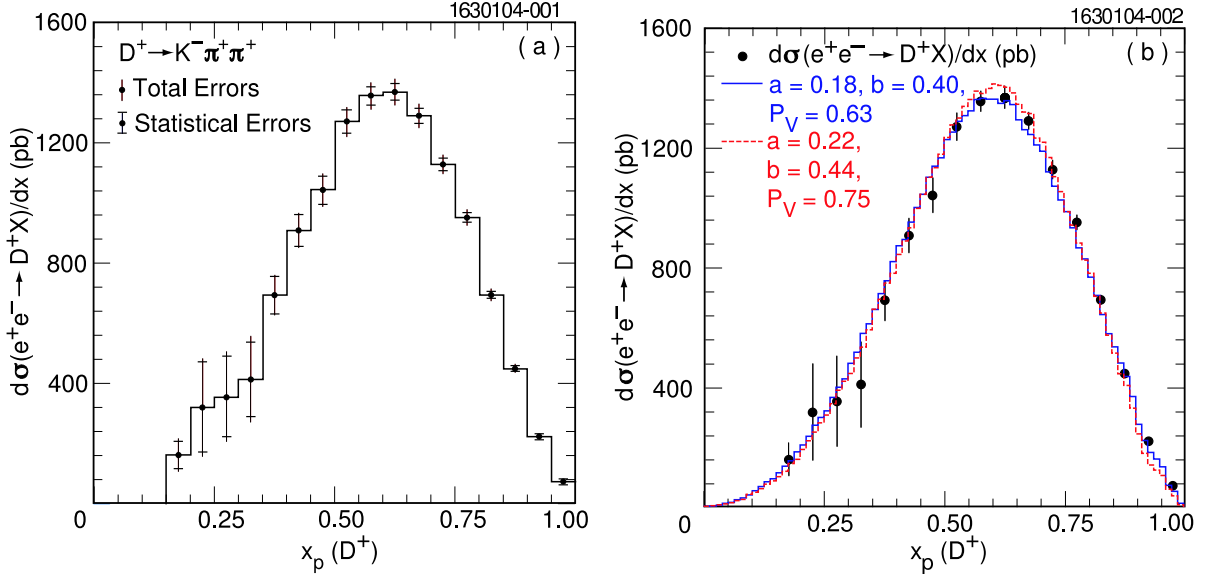


FIG. 7: Differential cross section  $d\sigma(e^+e^- \rightarrow D^+X)/dx_p$  in pb from the  $D^+ \rightarrow K^-\pi^+\pi^+$  decay mode. (a) shows explicitly the total and statistical errors. (b) the same spectrum overlaid with the JETSET spectra generated with two different sets of parameters (Sec. V).

## B. $D^0$ Spectrum

### 1. $D^0$ Spectrum from $D^0 \rightarrow K^- \pi^+$

Fig. 8 shows examples of fits to the  $M_{cand}$  distributions in three representative  $x_p$  bins, using fully smoothed parameters.

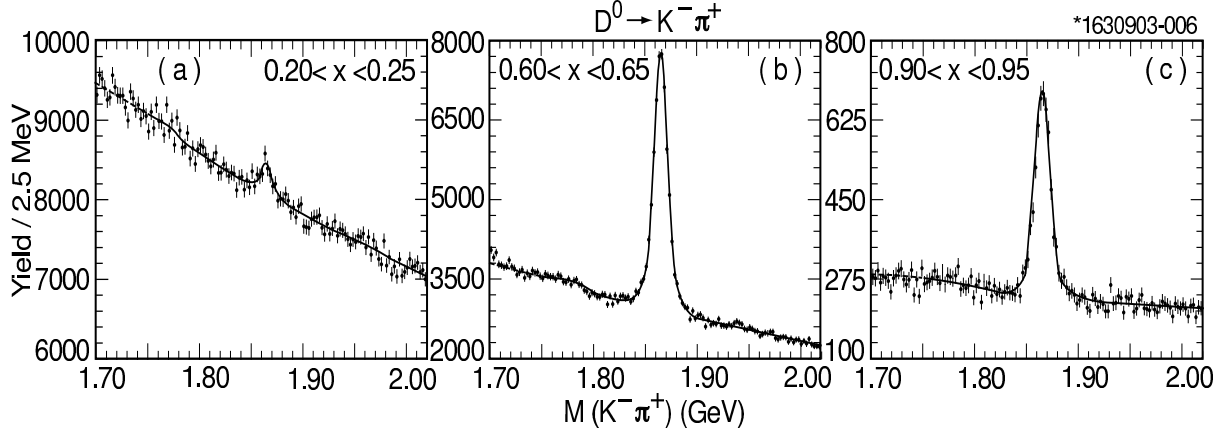


FIG. 8: Three examples of  $M(K^- \pi^+)$  distribution fits. Notice the large y offsets.

The  $D^0$  inclusive, differential production cross section obtained from this decay mode is shown in Fig. 9 and in App. B, Table VI, where the two systematic errors are listed. It is the simple average of three spectra obtained after smoothing the  $x_p$  dependence of the double Gaussian shape parameters in different smoothing sequences.

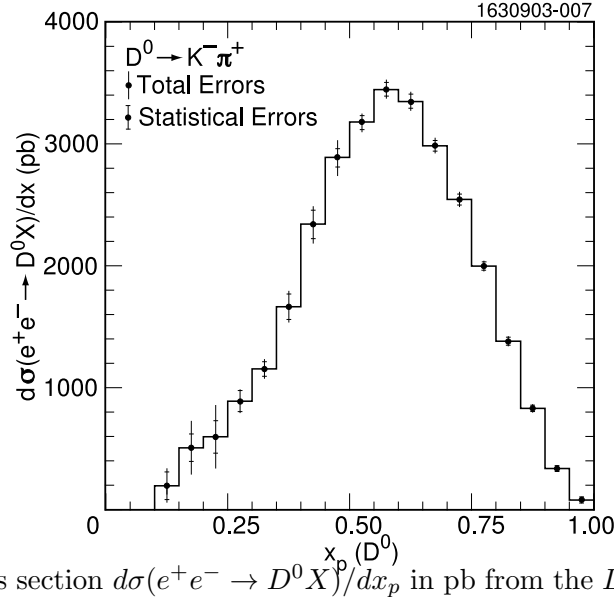


FIG. 9: Differential cross section  $d\sigma(e^+e^- \rightarrow D^0 X)/dx_p$  in pb from the  $D^0 \rightarrow K^- \pi^+$  decay mode.

2.  $D^0$  Spectrum from  $D^0 \rightarrow K^- \pi^+ \pi^+ \pi^-$

Fig. 10 shows examples of fits to the  $M_{cand}$  distributions in three representative  $x_p$  bins, with no parameter smoothing. Because of the large statistical errors, we find the Gaussian parameter smoothing procedure to be unreliable. However, as discussed in Sec. IID 2, for this mode we use also the COUNT method with three different widths of the excluded signal region in order to get part of the systematic error on this procedure.

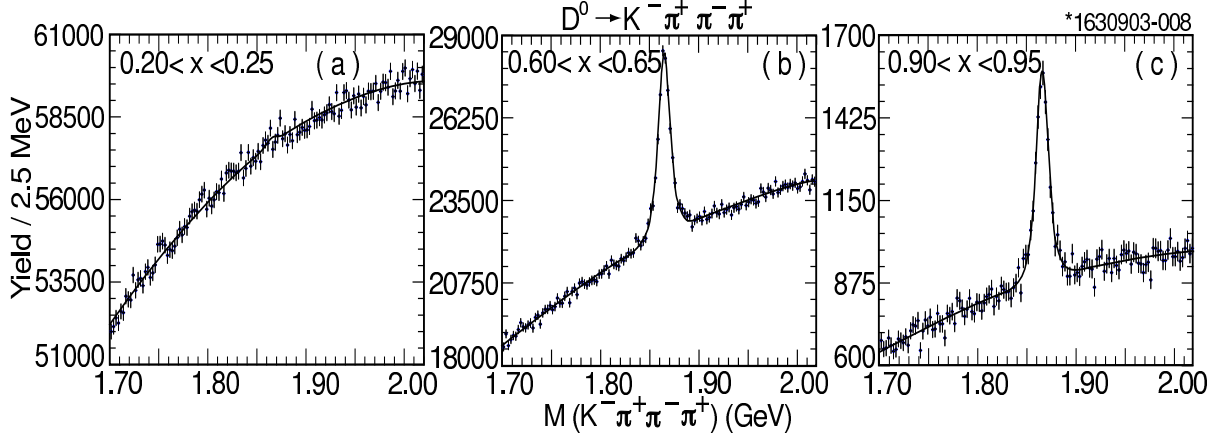


FIG. 10: Three examples of  $M(K^- \pi^+ \pi^+ \pi^-)$  distribution fits. Notice the large y offsets.

The  $D^0$  inclusive, differential production cross section obtained from this decay mode is shown in Fig. 11 and tabulated in App. B, Table VII, where the two systematic errors are listed. It is the average of the one obtained by double Gaussian fits (without any Gaussian parameter smoothing) and the one produced with the COUNT procedure, excluding from the background fit the 1.820-1.910 GeV region.

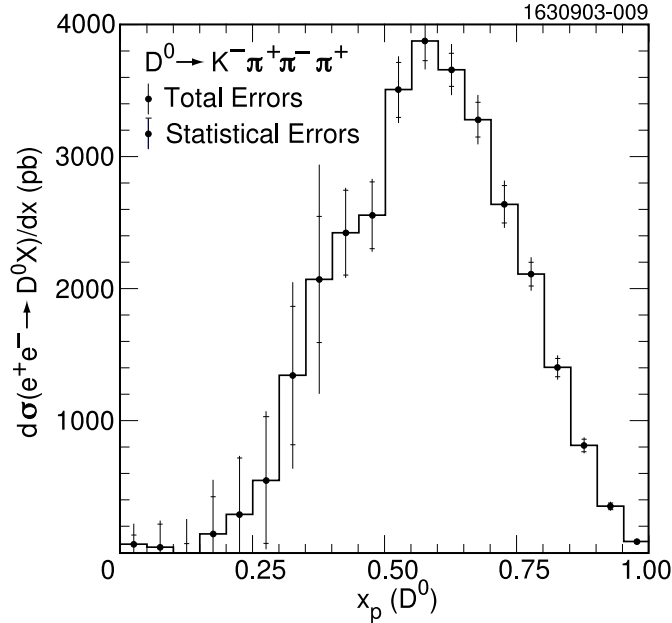


FIG. 11: Differential cross section  $d\sigma(e^+e^- \rightarrow D^0 X)/dx_p$  in pb from the  $D^0 \rightarrow K^- \pi^+ \pi^+ \pi^-$  decay mode.

### 3. The Average $D^0$ Spectrum

The weighted average of the spectra obtained from the two  $D^0$  decay modes analyzed is shown in Fig. 12 and tabulated in App. B, Table XII. The two JETSET generated spectra are explained in Sec. V.

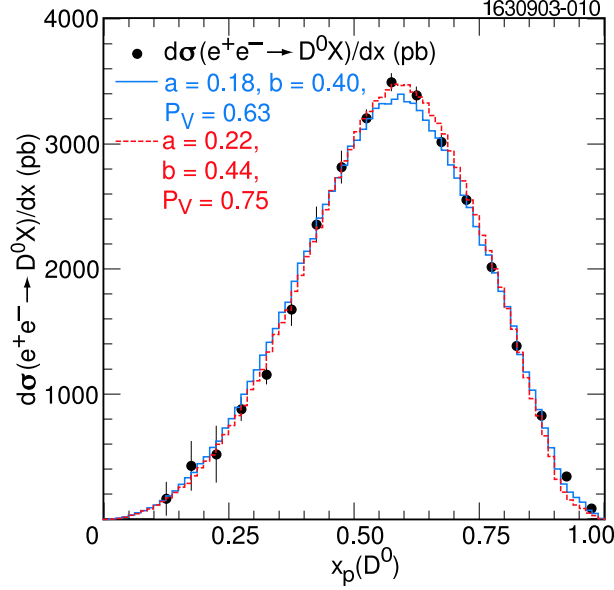


FIG. 12: Differential cross section  $d\sigma(e^+e^- \rightarrow D^0X)/dx_p$ , weighted average of the spectra from the  $D^0 \rightarrow K^-\pi^+$  and  $D^0 \rightarrow K^-\pi^+\pi^+\pi^-$  decay modes, overlaid with the JETSET spectra generated with two different sets of parameters (Sec. V).

### C. The $D^{*+}$ Spectrum

In Sec. IID we described our procedure for selecting  $D^{*+}$  candidates. The difference between the two  $M_{cand}$  distributions shown in Fig. 1 eliminates random  $D^0\pi^+$  associations.

#### 1. $D^{*+}$ Spectrum from $D^{*+} \rightarrow D^0\pi^+ \rightarrow (K^-\pi^+)\pi^+$

The subtracted  $M_{cand}$  distribution (Fig. 13) shows the additional backgrounds present in this  $D^0$  decay mode. They have been handled as described in Sec. IID 1.

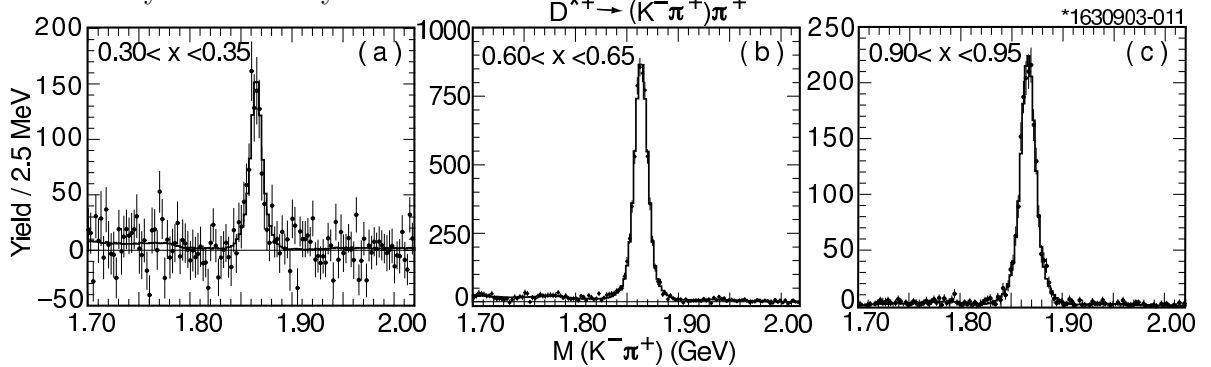


FIG. 13: Three examples of fits of the subtracted  $M(K^-\pi^+)$  distributions for  $D^{*+} \rightarrow D^0\pi^+ \rightarrow (K^-\pi^+)\pi^+$  candidates.

The spectrum is shown in Fig. 14 and tabulated in App. B, Table VIII, where the two systematic errors are listed. It is the one obtained after smoothing the  $x_p$  dependence of the double Gaussian shape parameters that gave the best CL in the gMC check (Sec. III).

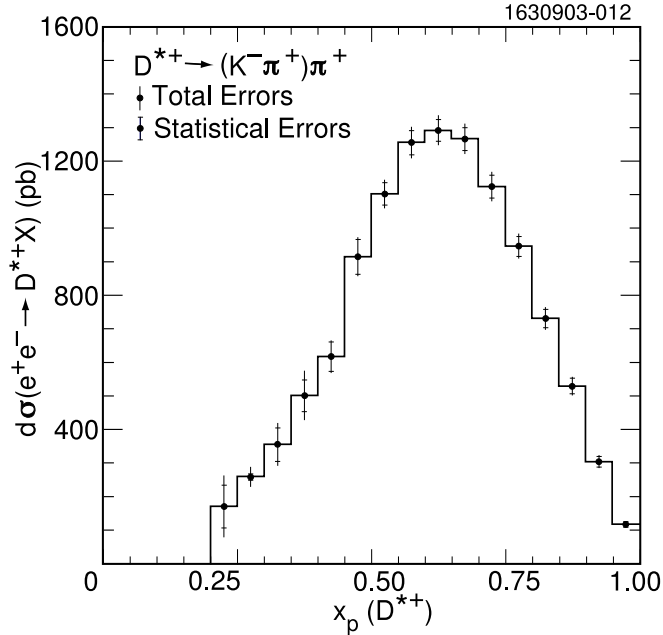


FIG. 14:  $d\sigma(e^+e^- \rightarrow D^{*+}X)/dx_p$ , from the  $D^{*+} \rightarrow D^0\pi^+ \rightarrow (K^-\pi^+)\pi^+$  decay mode.

## 2. $D^{*+}$ Spectrum from $D^{*+} \rightarrow D^0\pi^+ \rightarrow (K^-\pi^+\pi^+\pi^-\pi^+)$

Just as in the case of  $D^0 \rightarrow K^-\pi^+\pi^+\pi^-$ , taking advantage of the narrowness of the signal over a background smooth and well determined over a large region, we use the COUNT procedure described in Sec. IID2 with the signal region exclusion as optimized in that analysis (1.820-1.910 GeV). The  $Q$  selection reduces drastically the background with respect the  $D^0$  case, and we obtain good double Gaussian fits of the signal as shown, for three representative  $x_p$  bins, in Fig. 15.

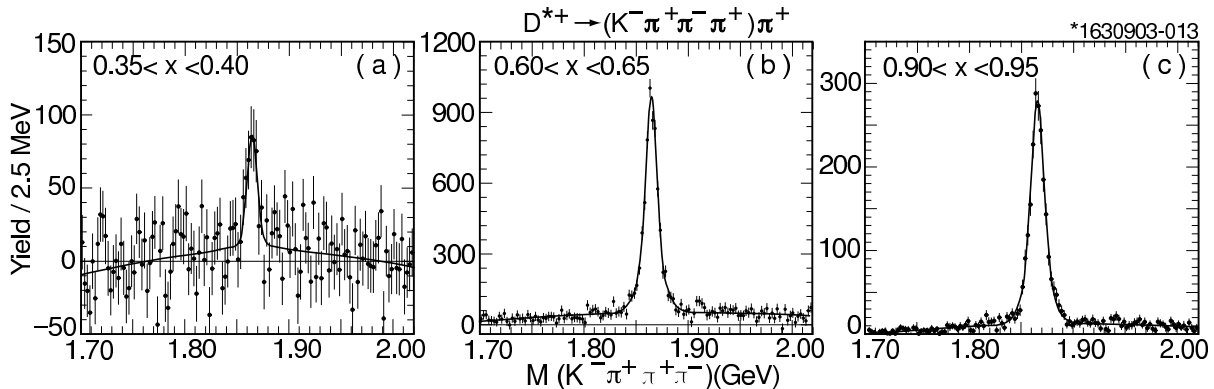


FIG. 15: Three examples of fits of the subtracted  $M(K^-\pi^+\pi^-\pi^+)$  distributions for  $D^{*+} \rightarrow D^0\pi^+ \rightarrow (K^-\pi^+\pi^+\pi^-\pi^+)$  candidates.

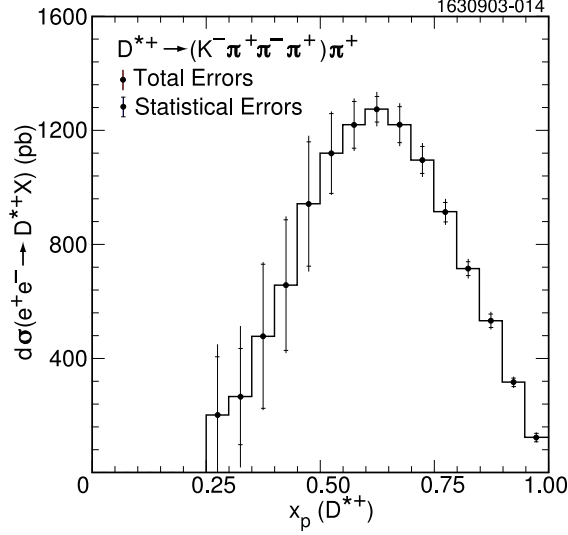


FIG. 16:  $d\sigma(e^+e^- \rightarrow D^{*+}X)/dx_p$  from the  $D^{*+} \rightarrow D^0\pi^+ \rightarrow (K^-\pi^+\pi^-\pi^+)\pi^+$  decay mode.

The spectrum is shown in Fig. 16 and tabulated in App. B, Table IX, where the two systematic errors are listed. It is the one obtained using a double Gaussian (with fully smoothed parameters) to fit the signal.

### 3. The Average $D^{*+}$ Spectrum

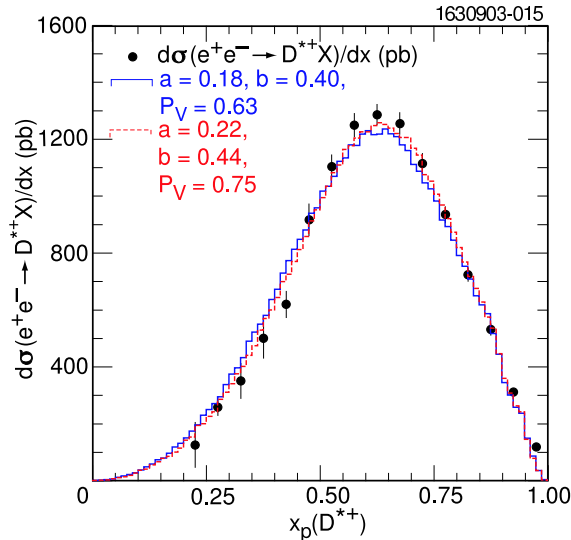


FIG. 17: Differential cross section  $d\sigma(e^+e^- \rightarrow D^{*+}X)/dx_p$ , weighted average of  $D^{*+} \rightarrow D^0\pi^+ \rightarrow (K^-\pi^+)\pi^+$  and  $D^{*+} \rightarrow D^0\pi^+ \rightarrow (K^-\pi^+\pi^-\pi^+)\pi^+$  spectra, overlaid with the JETSET spectra generated with two sets of parameters (Sec. V).

The weighted average of the spectra obtained from the two decay modes analyzed is shown in Fig. 17 and tabulated in App. B, Table XII. The two JETSET generated spectra are explained in Sec. V.

## D. $D^{*0}$ Spectrum

To suppress random  $D^0\pi^0$  associations, we use the subtraction procedure already used for the  $D^{*+}$  cases and illustrated in Fig. 1.

### 1. $D^{*0}$ Spectrum from $D^{*0} \rightarrow D^0\pi^0 \rightarrow (K^-\pi^+)\pi^0$

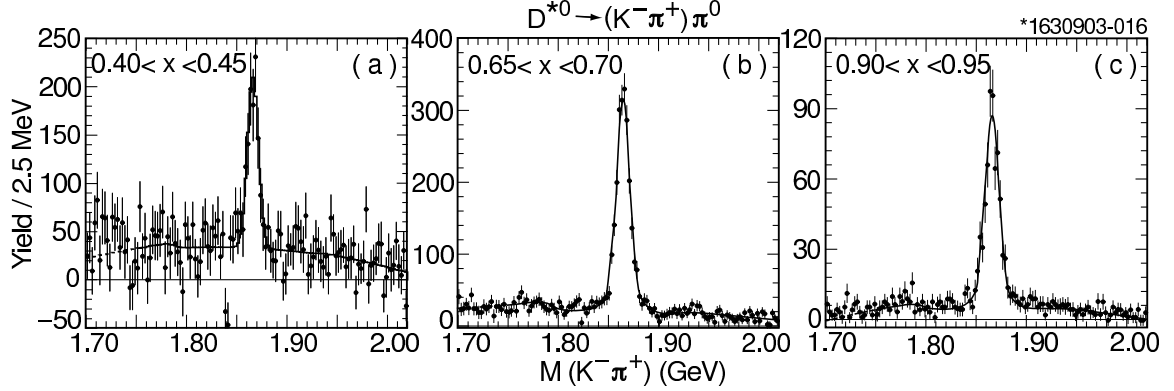


FIG. 18: Three examples of fits of the  $M(K^-\pi^+)$  distributions for  $D^{*0} \rightarrow D^0\pi^0 \rightarrow (K^-\pi^+)\pi^0$  candidates. Fully smoothed Gaussian parameters.

Fig. 18 shows three examples of fits of the subtracted  $M_{cand}$  distribution for this channel. Here too we add to the fitting functions the backgrounds described in Sec. IID 1.

The differential cross section is shown in Fig. 19 and tabulated in in App. B, Table X, where the two systematic errors are listed. Among the three variations of the procedure to smooth the Gaussian parameters (see Sec. IIF) we choose the one that gives the best CL in the gMC check (Sec. III).

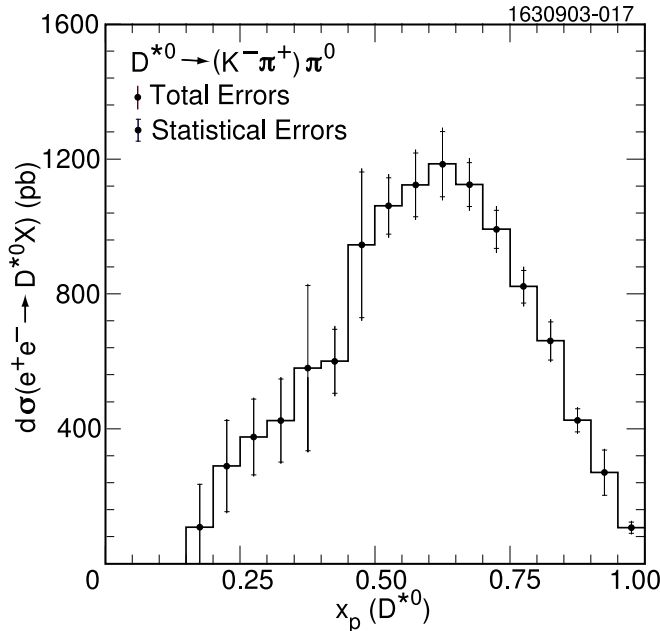


FIG. 19:  $d\sigma(e^+e^- \rightarrow D^{*0}X)/dx_p$ , from the  $D^{*0} \rightarrow D^0\pi^0 \rightarrow (K^-\pi^+)\pi^0$  decay mode.

2.  $D^{*0}$  Spectrum from  $D^{*0} \rightarrow D^0 \pi^0 \rightarrow (K^- \pi^+ \pi^- \pi^+) \pi^0$

Fig. 20 shows, for three representative  $x_p$  bins, the fits of the subtracted  $M_{cand}$  distribution, using a double Gaussian and a polynomial background.

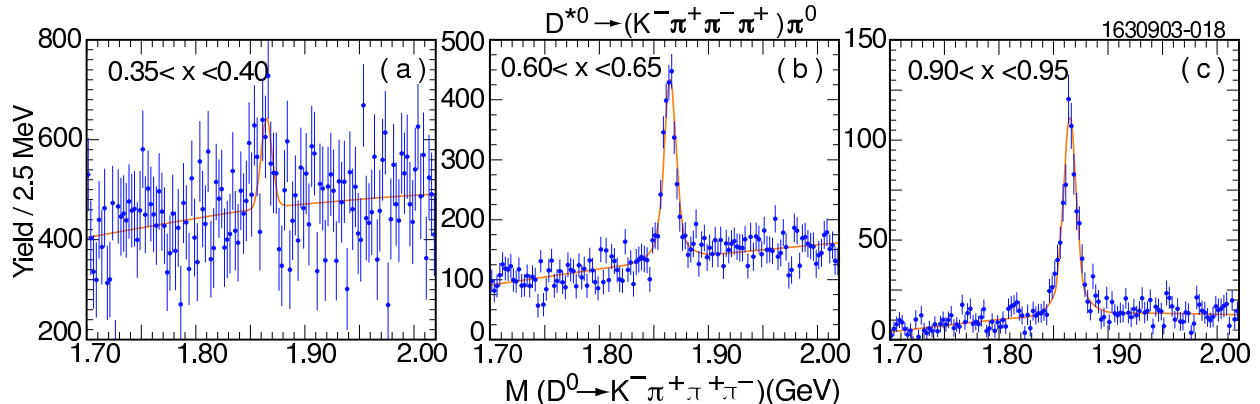


FIG. 20: Three examples of fits of the subtracted  $M(K^- \pi^+ \pi^- \pi^+)$  distributions for  $D^{*0} \rightarrow D^0 \pi^0 \rightarrow (K^- \pi^+ \pi^- \pi^+) \pi^0$  candidates.

Because of the smaller decay branching ratio and the smaller detection efficiency, due to the presence of a  $\pi^0$ , the statistical errors are quite large, especially for  $x_p < 0.50$ , where we can use only the continuum events. We have used both the COUNT procedure and the double Gaussian signal fitting (without parameter smoothing) to get the  $D^{*0}$  yield.

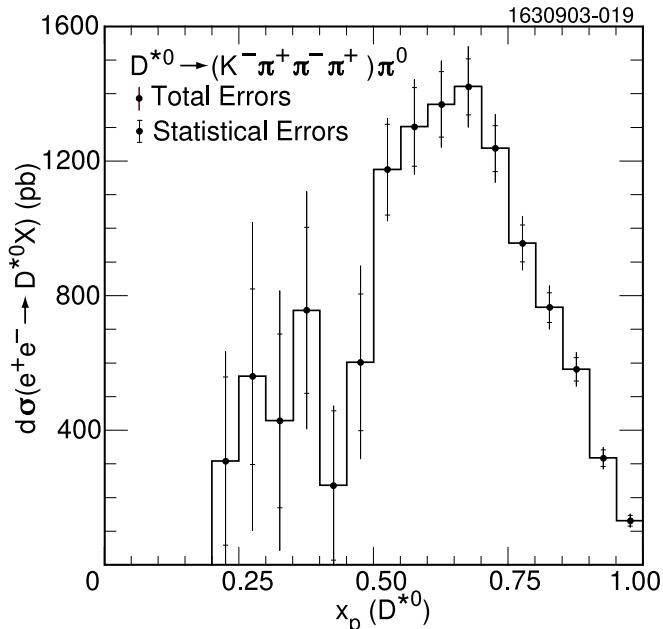


FIG. 21:  $d\sigma(e^+e^- \rightarrow D^{*0}X)/dx_p$ , from the  $D^{*0} \rightarrow D^0 \pi^0 \rightarrow (K^- \pi^+ \pi^- \pi^+) \pi^0$  decay mode.

The spectrum is shown in Fig. 21 and tabulated in App. B, Table XI, where the two systematic errors are listed. It is the simple average of that obtained by fitting the signal with the double Gaussian (smoothed parameters) and the one obtained by the COUNT method using the signal region exclusion optimized in that analysis (1.820-1.910 GeV).

### 3. The Average $D^{*0}$ Spectrum

The weighted average of the spectra obtained from the two decay modes analyzed is shown in Fig. 22 and listed in App. B, Table XII. The two JETSET generated spectra are explained in Sec. V.

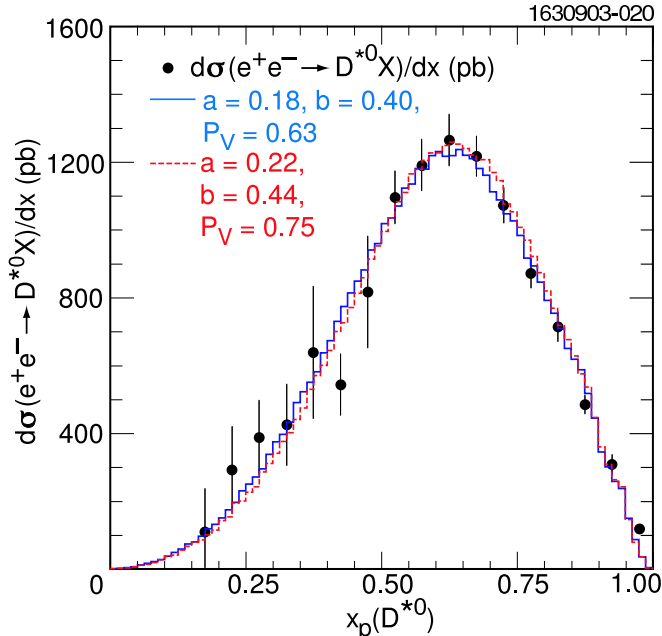


FIG. 22:  $d\sigma(e^+e^- \rightarrow D^{*0}X)/dx_p$ , weighted average of the  $D^{*0} \rightarrow D^0\pi^0 \rightarrow (K^-\pi^+)\pi^0$  and  $D^{*0} \rightarrow D^0\pi^0 \rightarrow (K^-\pi^+\pi^+\pi^-)\pi^0$  decay modes. Overlaid are the JETSET spectra generated with two sets of parameters (Sec. V).

## IV. TOTAL CROSS SECTIONS AND AVERAGE $x_p$

The total production cross sections for each channel are shown in Table III. They are calculated by summing each differential cross section bin-by-bin and combining in quadrature the statistical errors in each bin, the first error in the table. If the yield in the lowest few bins cannot be reliably measured, the total cross section is corrected by extrapolating the spectrum to  $x_p = 0$  using the JETSET distribution that fits the spectrum, discussed in Sec. V. This correction is between 0.2% and 6%.

In Table II we list, channel by channel, the components of the systematic error on the total production cross sections. In the first column we report the rms spread of the total cross sections obtained by the four or five procedures used for each channel. We consider as systematic error the discrepancy between the areas of the input and reconstructed spectra in the gMC check (Sec. III). This is shown in the second column. In the third column we list the percent difference between the integral of the spectra obtained using the double Gaussian and the one that uses the TAGMC signal shape (Sec. IID). This error is not considered for the channels where the  $D^0$  decays to  $K^-\pi^+\pi^+\pi^-$ , because of the use of the COUNT procedure for those channels. We assume a 10% error on the extrapolation and show it in column 4. We estimate a 1% per track uncertainty in the charged track detection efficiency

and 0.8% per track for particle identification efficiency. The  $\pi^0$  detection uncertainty is estimated to be 3% per  $\pi^0$ . The choice of track quality and geometrical cuts result in an error of 0.5% also per track. The per track errors are multiplied by the number of tracks in the decay. As discussed in Sec. II J, we attribute a 0.5% error due to possible inaccuracies in the Monte Carlo simulation of the initial state radiation. The error on the integrated luminosity is estimated as 1.9%.

TABLE II: Systematic errors described in the text. Some are listed as percent of the cross section, other ones directly in pb. The momentum dependent systematic errors are listed also in the tables in App. B. The error due to the uncertainty on the branching ratio is shown only in Table III.

Decay channel	procedures rms	gMC check	signal shape	Extra- polat.	track det.eff.	part. ID	$\pi^0$ det.	other sel.	ISR sim.	Lum.
$D^+ \rightarrow K^- \pi^+ \pi^+$	5pb	15pb	1.6%	0.5pb	3%	2.4%		1.5%	0.5%	1.9%
$D^0 \rightarrow K^- \pi^+$	22pb	8pb	1.6%	0.4pb	2%	1.6%		1.0%	0.5%	1.9%
$D^0 \rightarrow K^- \pi^+ \pi^+ \pi^-$	41pb	29pb		3.2pb	4%	3.2%		2.0%	0.5%	1.9%
$D^{*+} \rightarrow (K^- \pi^+) \pi^+$	8pb	15pb	1.6%	0.9pb	3%	2.4%		1.5%	0.5%	1.9%
$D^{*+} \rightarrow (K^- \pi^+ \pi^+ \pi^-) \pi^+$	17pb	7pb		3.3pb	5%	4.0%		2.5%	0.5%	1.9%
$D^{*0} \rightarrow (K^- \pi^+) \pi^0$	11pb	10pb	1.6%	3.6pb	2%	1.6%	3%	1.0%	0.5%	1.9%
$D^{*0} \rightarrow (K^- \pi^+ \pi^+ \pi^-) \pi^0$	45pb	12pb		1.1pb	4%	3.2%	3%	2.0%	0.5%	1.9%

These systematic errors are combined in quadrature to give the systematic error on the total cross section, the second entry in Table III.

TABLE III: Total production cross sections and average  $x_p$ , as derived from each decay mode. The cross section errors are, in this order, the statistical error, the systematic error and the error due to the uncertainty on the branching ratio.

Decay channel	Total Cross Section (pb) at 10.5 GeV C.M.E.
$D^+ \rightarrow K^- \pi^+ \pi^+$	$\sigma(e^+ e^- \rightarrow D^+ X) = 640 \pm 14 \pm 35 \pm 43$
$D^0 \rightarrow K^- \pi^+$	$\sigma(e^+ e^- \rightarrow D^0 X) = 1,521 \pm 16 \pm 62 \pm 36$
$D^0 \rightarrow K^- \pi^+ \pi^+ \pi^-$	$\sigma(e^+ e^- \rightarrow D^0 X) = 1,579 \pm 55 \pm 102 \pm 63$
$D^{*+} \rightarrow D^0 \pi^+ \rightarrow (K^- \pi^+) \pi^+$	$\sigma(e^+ e^- \rightarrow D^{*+} X) = 583 \pm 8 \pm 33 \pm 14$
$D^{*+} \rightarrow D^0 \pi^+ \rightarrow (K^- \pi^+ \pi^+ \pi^-) \pi^+$	$\sigma(e^+ e^- \rightarrow D^{*+} X) = 572 \pm 26 \pm 45 \pm 24$
$D^{*0} \rightarrow D^0 \pi^0 \rightarrow (K^- \pi^+) \pi^0$	$\sigma(e^+ e^- \rightarrow D^{*0} X) = 559 \pm 24 \pm 35 \pm 29$
$D^{*0} \rightarrow D^0 \pi^0 \rightarrow (K^- \pi^+ \pi^+ \pi^-) \pi^0$	$\sigma(e^+ e^- \rightarrow D^{*0} X) = 616 \pm 32 \pm 62 \pm 39$

We calculate  $\langle x_p \rangle$  for the  $D^+$  spectrum and for the spectra of  $D^0$ ,  $D^{*+}$  and  $D^{*0}$  averaged over the decay modes. We supplement the data spectrum in the lowest bins using the JETSET spectra normalized to the spectra. We take the errors on these ‘‘borrowed’’ cross sections to be roughly comparable to the data in nearby bins. The results are shown in Table IV.

## V. OPTIMIZATION OF JETSET PARAMETERS

Largely for internal use of our collaboration, we perform a simple fit of the  $D^0$  spectrum (from the  $D^0 \rightarrow K^- \pi^+$  decay mode) varying the three JETSET parameters that are most

TABLE IV:  $\langle x_p \rangle$  for the four charm mesons considered. The first error is statistical, the second systematic.

Meson	$\langle x_p \rangle$	Meson	$\langle x_p \rangle$
$D^+$	$0.582 \pm 0.008 \pm 0.004$	$D^{*+}$	$0.611 \pm 0.007 \pm 0.004$
$D^0$	$0.570 \pm 0.005 \pm 0.004$	$D^{*0}$	$0.596 \pm 0.009 \pm 0.004$

important for the shape of the spectrum. The first and second are the parameters  $a$  and  $b$  appearing in the ‘‘Lund Symmetric Fragmentation Function’’ [21, 22]:

$$f(z) = N \frac{(1-z)^a}{z} \exp \left[ \frac{-b \cdot m_{\perp}^2}{z} \right] \quad (1)$$

where  $z$  is the reduced energy  $x_E$ , or momentum  $x_p$ , of the hadron and  $m_{\perp}^2 = m^2 + p_{\perp}^2$ , with  $m$  being the hadron mass and  $p_{\perp}$  the component of the hadron momentum perpendicular to the jet axis.

The third parameter is the probability  $P_V$  that a meson of given flavor be generated as a vector meson, rather than pseudoscalar or tensor,  $P_V \equiv V/(P + V + T)$ . The data indicate, as expected, that the majority of  $D^0$ 's are not produced directly in the fragmentation of the charm quark, but from the decay of  $D^*$ 's. In JETSET [24] these parameters are PARJ(41), PARJ(42) and PARJ(13).

The result of the fit of the  $D^0$  spectrum (in the  $K^- \pi^+$  decay mode) is:

$$a = 0.178 \pm 0.007, \quad b = 0.393 \pm 0.006, \quad P_V = 0.627 \pm 0.015.$$

Keeping  $P_V$  fixed at the naive value  $P_V = 0.75$ , we obtain  $a = 0.223 \pm 0.009$  and  $b = 0.438 \pm 0.005$ . In both cases the quoted errors are simple statistical errors. Correlation between parameters are not evaluated. The spectra resulting from these parametrizations are shown in Fig. 7, 12, 17, 22.

Notice that we do not consider our results of  $D^+$ ,  $D^{*+}$  and  $D^{*0}$  spectra in the optimization process. However, *a posteriori* we see, visually from the figures, that the spectra generated with these parameters seem to reproduce rather accurately also the  $D^+$ ,  $D^{*+}$  and  $D^{*0}$  experimental distributions. However, it is not obvious which one of the two sets should be preferred. Furthermore, these parameters, while useful for the Monte Carlo simulation of  $D$  and  $D^*$  spectra at the c.m. energy of our and similar experiments, should not be taken as having general validity and theoretical significance. In fact, the  $D_s^+$  spectrum generated by JETSET with our fitted parameters disagrees appreciably with the spectrum measured by the CLEO [32] and BaBar [33] collaborations. It should be noted that the effect of these parameters may also be influenced by the value of other JETSET parameters.

## VI. CONCLUSIONS

We have measured the momentum distribution of  $D^0$ ,  $D^+$ ,  $D^{*+}$  and  $D^{*0}$  produced in non-resonant  $e^+e^-$  annihilation at a CME of about 10.5 GeV. These distributions can be used to guide and check QCD calculations of fragmentation functions needed to predict heavy meson production in both  $e^+e^-$  annihilation and hadron collisions at very high energy. These

distributions have also been used to determine the JETSET parameters that best reproduce these distributions.

### Acknowledgments

We gratefully acknowledge the effort of the CESR staff in providing us with excellent luminosity and running conditions. G. Moneti thanks M. Cacciari and P. Nason for very useful discussions on QCD calculations of heavy flavour fragmentation. M. Selen thanks the Research Corporation, and A.H. Mahmood thanks the Texas Advanced Research Program. This work was supported by the National Science Foundation and the U.S. Department of Energy.

- 
- [1] G. Alexander *et al.* [OPAL Collaboration], Phys. Lett. **B364**, 93 (1995).
  - [2] K. Abe *et al.* [SLD Collaboration], Phys. Rev. Lett. **84**, 4300 (2000) [arXiv:hep-ex/9912058].
  - [3] A. Heister *et al.* [ALEPH Collaboration], Phys. Lett. **B512**, 30 (2001) [arXiv:hep-ex/0106051].
  - [4] B. Adeva *et al.* [L3 Collaboration], Phys. Lett. **B261**, 177 (1991).
  - [5] H. Albrecht *et al.* [ARGUS Collaboration], Z. Phys. **C52**, 353 (1991).
  - [6] D. Bortoletto *et al.* [CLEO Collaboration], Phys. Rev. **D37**, 1719 (1988).
  - [7] O. Biebel, P. Nason, B.R. Webber [arXiv:hep-ph/0109282] v2, an abbreviated version is in [29].
  - [8] P. Nason and B. R. Webber, Nucl. Phys. **B421**, 473 (1994) [Erratum-ibid. **B480**, 755 (1996)].
  - [9] E. Ben-Haim *et al.*, [arXiv:hep-ph/0302157].
  - [10] M. Cacciari and S. Catani, Nucl. Phys. **B617**, 253 (2001) [arXiv:hep-ph/0107138].
  - [11] B. Abbott *et al.* [D0 Collaboration], Phys. Lett. **B487**, 264 (2000).
  - [12] D. Acosta *et al.* [CDF Collaboration], Phys. Rev. **D65**, 052005 (2002).
  - [13] D. Acosta *et al.* [CDF Collaboration], Phys. Rev. Lett. **91**, 241804 (2003) [arXiv:hep-ex/0307080].
  - [14] S. Aid *et al.* [H1 Collaboration], Z. Phys. **C72**, 593 (1996).
  - [15] S. Chekanov *et al.* [ZEUS Collaboration], [arXiv:hep-ex/0308068].
  - [16] M. Cacciari and E. Gardi, Nucl. Phys. **B664**, 299 (2003) [arXiv:hep-ph/0301047].
  - [17] G. Altarelli and G. Parisi, Nucl. Phys. **B126**, 298 (1977).
  - [18] W. Furmanski and R. Petronzio, Phys. Lett. **B97**, 437 (1980).
  - [19] R. Barate *et al.* [ALEPH Collaboration], Eur. Phys. J. **C16**, 597-611 (2000) [arXiv:hep-ex/9909032].
  - [20] X. Artru, G. Menessier, Nucl. Phys. **70**, 93 (1974).
  - [21] Bo Andersson *et al.*, Phys. Reports **97**, 31 (1983).
  - [22] Bo Andersson, "The Lund Model", Cambridge U. Press (1998).
  - [23] G. Marchesini *et al.*, Comp. Phys. Comm. **67**, 465 (1992); G. Corcella *et al.*, JHEP **0101**, 010 (2001).
  - [24] T. Sjostrand, Comp. Phys. Comm. **82**, 74-89, (1994), T. Sjostrand, "PYTHIA 5.7 and JETSET 7.4 Physics and Manual" [hep-ph/9508391].
  - [25] S. Chun and C. Buchanan, Phys. Reports **292**, 239 (1998).

- [26] Y. Kubota *et al.* [CLEO Collaboration], Nucl. Instrum. Methods Phys. Res., Sec. A **320**, 66(1992).
- [27] T. Hill *et al.* [CLEO Collaboration], Nucl. Instrum. Methods Phys. Res., Sec. A **418**, 32(1998).
- [28] L. Gibbons *et al.* [CLEO Collaboration], Phys. Rev. **D56**, 3783 (1997).
- [29] D. E. Groom *et al.* [PDG], Eur. Phys. Jour. **15**, 1, (2000) and K. Hagiwara *et al.* [PDG], Phys. Rev. **66**, 010001-1 2002.
- [30] T. Sjöstrand, Comp. Phys. Comm. **39**, 347 (1986), T. Sjöstrand, M. Bengtson, Comp. Phys. Comm. **43**, 367 (1987).
- [31] R. Brun *et al.*, “GEANT, Detector Description and Simulation Tool”, CERN Program Library Long Writeup W5013, 1993.
- [32] R. A. Briere *et al.* [CLEO Collaboration], Phys. Rev. **D62**, 072003 (2000).
- [33] B. Aubert *et al.* [BABAR Collaboration], Phys. Rev. **D65** (2002) 091104 [hep-ex/0201041].

## APPENDIX A: PLOTS OF DETECTION EFFICIENCIES VS $x_p$

In the following figures we show the detection efficiency dependence on  $x_p$  for all the mesons and decay modes analyzed. The detection efficiencies obtained from the signal and generic MC simulations are plotted, together with the curve resulting from the fit of their weighted average to a polynomial.

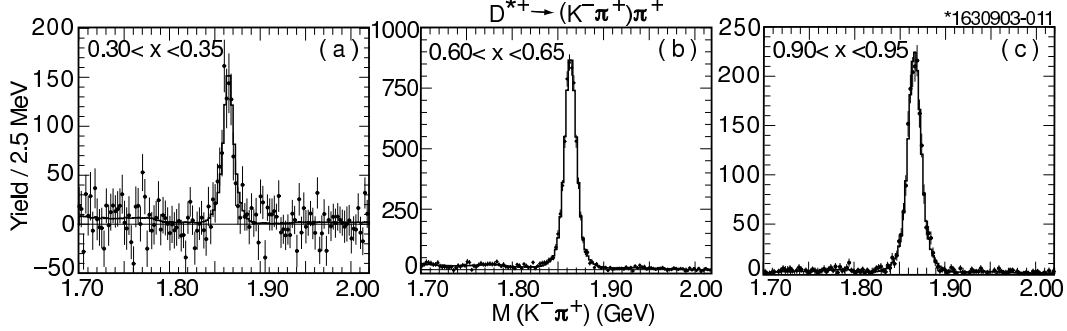


FIG. 23: Direct comparison of the detection efficiencies from signal and generic Monte Carlo and the result of smoothing their average: (a) for the  $D^{*+} \rightarrow K^- \pi^+ \pi^+$  channel, (b) for the  $D^{*0} \rightarrow K^- \pi^+$  channel, and (c) for the  $D^0 \rightarrow K^- \pi^+ \pi^+ \pi^-$  channel.

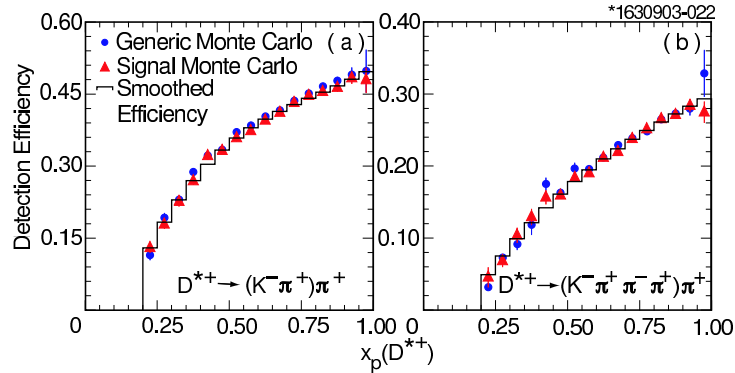


FIG. 24: Comparison of the detection efficiencies obtained from the signal and generic Monte Carlo and their smoothed average: (a) for the  $D^{*+} \rightarrow D^0 \pi^+ \rightarrow (K^- \pi^+) \pi^+$  channel, (b) for the  $D^{*+} \rightarrow D^0 \pi^+ \rightarrow (K^- \pi^+ \pi^- \pi^+) \pi^+$  channel.

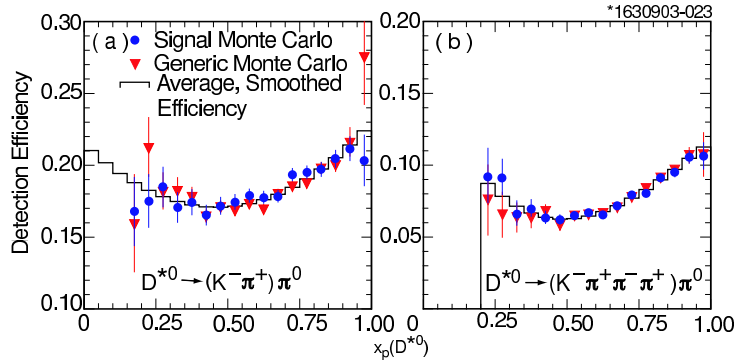


FIG. 25: Comparison of the unsmoothed detection efficiencies obtained from the signal and generic Monte Carlo: (a) for the  $D^{*0} \rightarrow D^0 \pi^0 \rightarrow (K^- \pi^+) \pi^0$ , (b) for the  $D^{*0} \rightarrow D^0 \pi^0 \rightarrow (K^- \pi^+ \pi^- \pi^+) \pi^0$  channel.

## APPENDIX B: TABLES OF DIFFERENTIAL CROSS SECTIONS

In the following tables, we report the quantity  $d\sigma/dx_p$  in pb. Notice that the systematic and total errors are errors on the bin content (*i.e.*, the first column). The first column of systematic errors is obtained from the rms spread of yields for the different procedures used to calculate the spectrum. The second column of systematic errors is derived from the “gMC check” described in Sec. III. These are the errors relevant to the shape of the spectra, *i.e.*, they do not include the systematic errors that are common to the whole momentum range and that contribute to the error on the total cross section (Sec. IV).

TABLE V:  $d\sigma(e^+e^- \rightarrow D^+X)/dx_p$  in pb; ( $D^+ \rightarrow K^- \pi^+ \pi^+$ )

$x_p$	$d\sigma/dx_p$ (pb)	Statistical	Errors (pb)		Total
			Systematic		
0.15-0.20	161	47	27	3	54
0.20-0.25	320	153	53	5	162
0.25-0.30	356	137	59	6	149
0.30-0.35	413	126	68	7	143
0.35-0.40	693	65	11	11	67
0.40-0.45	909	55	14	15	59
0.45-0.50	1042	50	16	17	55
0.50-0.55	1271	40	20	21	49
0.55-0.60	1357	33	21	22	45
0.60-0.65	1370	29	21	22	42
0.65-0.70	1291	27	20	21	39
0.70-0.75	1129	22	17	18	34
0.75-0.80	952	18	15	16	28
0.80-0.85	694	13	11	11	21
0.85-0.90	449	11	7	7	15
0.90-0.95	223	7	3	4	9
0.95-1.00	74	4	1	1	5

TABLE VI:  $d\sigma(e^+e^- \rightarrow D^0 X)/dx_p$  in pb; ( $D^0 \rightarrow K^- \pi^+$ ).

$x_p$	$d\sigma/dx_p$ (pb)	Errors (pb)			Total
		Statistical	Systematic		
0.10-0.15	196	117	73	1	138
0.15-0.20	507	115	188	3	220
0.20-0.25	597	136	221	3	256
0.25-0.30	891	88	37	5	96
0.30-0.35	1154	62	48	7	79
0.35-0.40	1665	106	70	10	128
0.40-0.45	2341	118	98	13	155
0.45-0.50	2889	78	121	17	145
0.50-0.55	3178	60	42	18	75
0.55-0.60	3444	59	45	20	77
0.60-0.65	3345	60	44	19	76
0.65-0.70	2984	46	39	17	62
0.70-0.75	2542	47	33	15	59
0.75-0.80	1997	37	26	11	47
0.80-0.85	1380	35	18	8	40
0.85-0.90	831	27	11	5	30
0.90-0.95	337	15	4	2	16
0.95-1.00	78	7	1	0.4	7

TABLE VII:  $d\sigma(e^+e^- \rightarrow D^0 X)/dx_p$  in pb; ( $D^0 \rightarrow K^- \pi^+ \pi^+ \pi^-$ ).

$x_p$	$d\sigma/dx_p$ (pb)	Statistical	Errors (pb)		
			Systematic	Total	
0.15-0.20	146	283	291	4	406
0.20-0.25	292	430	101	9	441
0.25-0.30	551	481	190	16	518
0.30-0.35	1343	525	464	40	702
0.35-0.40	2068	479	715	61	862
0.40-0.45	2420	323	60	72	337
0.45-0.50	2552	254	63	76	272
0.50-0.55	3500	211	86	104	250
0.55-0.60	3868	151	95	115	212
0.60-0.65	3651	127	90	108	190
0.65-0.70	3274	134	81	97	184
0.70-0.75	2635	143	65	78	175
0.75-0.80	2108	93	52	63	123
0.80-0.85	1403	71	35	42	89
0.85-0.90	815	49	20	24	59
0.90-0.95	355	27	9	11	31
0.95-1.00	87	12	2	3	13

TABLE VIII:  $d\sigma(e^+e^- \rightarrow D^{*+} X)/dx_p$  in pb; ( $D^{*+} \rightarrow (K^- \pi^+) \pi^+$ ).

$x_p$	$d\sigma/dx_p$ (pb)	Statistical	Errors (pb)		
			Systematic	Total	
0.20-0.25	169	65	65	1	92
0.25-0.30	258	11	27	2	29
0.30-0.35	355	51	38	3	63
0.35-0.40	501	49	53	4	72
0.40-0.45	617	45	12	5	47
0.45-0.50	915	53	18	7	57
0.50-0.55	1103	35	22	9	42
0.55-0.60	1256	37	25	10	46
0.60-0.65	1293	34	25	10	43
0.65-0.70	1267	35	25	10	44
0.70-0.75	1125	36	22	9	43
0.75-0.80	947	30	19	7	36
0.80-0.85	731	29	14	6	32
0.85-0.90	529	24	10	4	27
0.90-0.95	303	17	6	2	18
0.95-1.00	116	9	2	1	9

TABLE IX:  $d\sigma(e^+e^- \rightarrow D^{*+}X)/dx_p$  in pb; ( $D^{*+} \rightarrow (K^- \pi^+ \pi^+ \pi^-) \pi^+$ ).

$x_p$	$d\sigma/dx_p$ (pb)	Errors (pb)			Total
		Statistical	Systematic		
0.25-0.30	201	205	136	4	246
0.30-0.35	265	170	179	5	247
0.35-0.40	478	254	45	9	258
0.40-0.45	657	231	61	12	239
0.45-0.50	943	219	88	17	237
0.50-0.55	1121	141	27	20	145
0.55-0.60	1221	83	29	22	91
0.60-0.65	1276	46	30	23	60
0.65-0.70	1221	65	29	22	74
0.70-0.75	1096	49	26	20	59
0.75-0.80	915	35	22	17	45
0.80-0.85	715	26	17	13	34
0.85-0.90	533	25	13	10	30
0.90-0.95	317	16	8	6	18
0.95-1.00	122	16	3	2	16

TABLE X:  $d\sigma(e^+e^- \rightarrow D^{*0}X)/dx_p$  in pb; ( $D^{*0} \rightarrow (K^- \pi^+) \pi^0$ ).

$x_p$	$d\sigma/dx_p$ (pb)	Errors (pb)			Total
		Statistical	Systematic		
0.15-0.20	108	128	6	2	128
0.20-0.25	290	137	17	7	138
0.25-0.30	376	113	23	9	116
0.30-0.35	425	124	26	10	127
0.35-0.40	580	246	35	13	249
0.40-0.45	601	96	36	14	104
0.45-0.50	946	217	57	22	226
0.50-0.55	1061	85	30	24	93
0.55-0.60	1124	95	31	26	104
0.60-0.65	1186	98	33	27	107
0.65-0.70	1125	66	31	26	78
0.70-0.75	992	58	28	23	68
0.75-0.80	822	50	23	19	58
0.80-0.85	662	58	18	15	63
0.85-0.90	425	35	12	10	39
0.90-0.95	271	68	8	6	69
0.95-1.00	107	18	3	2	19

TABLE XI:  $d\sigma(e^+e^- \rightarrow D^{*0}X)/dx_p$  in pb; ( $D^{*0} \rightarrow (K^- \pi^+ \pi^+ \pi^-) \pi^0$ ).

$x_p$	$d\sigma/dx_p$ (pb)	Errors (pb)			Total
		Statistical	Systematic		
0.20-0.25	308	251	206	7	325
0.25-0.30	559	262	374	12	457
0.30-0.35	428	259	286	9	386
0.35-0.40	755	247	250	16	352
0.40-0.45	236	223	78	5	236
0.45-0.50	601	205	199	13	286
0.50-0.55	1173	135	64	25	152
0.55-0.60	1300	118	71	28	141
0.60-0.65	1367	100	75	29	128
0.65-0.70	1418	85	78	30	119
0.70-0.75	1235	70	68	27	101
0.75-0.80	954	56	52	21	80
0.80-0.85	764	46	42	16	64
0.85-0.90	581	36	32	12	50
0.90-0.95	317	26	17	7	32
0.95-1.00	131	18	7	3	20

TABLE XII: Differential cross sections  $d\sigma/dx_p$  in pb for  $D^+$ ,  $D^0$ ,  $D^{*+}$  and  $D^{*0}$ . The last three columns are weighted averaged over the two decay modes. The errors are the quadratic combination of the statistical and systematic errors, excluding the errors, discussed in Sec. IV, that affect the total cross section but not the shape of the spectrum.

$x_p$	$D^+$	$D^0$	$D^{*+}$	$D^{*0}$
0.10-0.15	-	162 $\pm$ 131	-	-
0.15-0.20	161 $\pm$ 54	425 $\pm$ 194	-	108 $\pm$ 128
0.20-0.25	320 $\pm$ 162	519 $\pm$ 224	124 $\pm$ 79	292 $\pm$ 127
0.25-0.30	356 $\pm$ 149	879 $\pm$ 94	257 $\pm$ 29	387 $\pm$ 112
0.30-0.35	413 $\pm$ 143	1156 $\pm$ 78	349 $\pm$ 61	425 $\pm$ 121
0.35-0.40	693 $\pm$ 67	1673 $\pm$ 126	499 $\pm$ 70	639 $\pm$ 203
0.40-0.45	909 $\pm$ 59	2355 $\pm$ 140	618 $\pm$ 46	542 $\pm$ 95
0.45-0.50	1042 $\pm$ 55	2814 $\pm$ 128	917 $\pm$ 55	814 $\pm$ 177
0.50-0.55	1271 $\pm$ 49	3205 $\pm$ 72	1104 $\pm$ 40	1092 $\pm$ 79
0.55-0.60	1357 $\pm$ 45	3493 $\pm$ 72	1249 $\pm$ 41	1186 $\pm$ 83
0.60-0.65	1370 $\pm$ 42	3388 $\pm$ 71	1287 $\pm$ 35	1260 $\pm$ 82
0.65-0.70	1291 $\pm$ 39	3014 $\pm$ 59	1255 $\pm$ 38	1212 $\pm$ 65
0.70-0.75	1129 $\pm$ 34	2552 $\pm$ 56	1115 $\pm$ 35	1068 $\pm$ 57
0.75-0.80	952 $\pm$ 28	2011 $\pm$ 44	934 $\pm$ 28	868 $\pm$ 47
0.80-0.85	694 $\pm$ 21	1384 $\pm$ 37	723 $\pm$ 23	712 $\pm$ 45
0.85-0.90	449 $\pm$ 15	828 $\pm$ 27	531 $\pm$ 20	484 $\pm$ 30
0.90-0.95	223 $\pm$ 9	341 $\pm$ 14	310 $\pm$ 13	309 $\pm$ 29
0.95-1.00	74 $\pm$ 5	80 $\pm$ 5	118 $\pm$ 8	119 $\pm$ 13

